

OPTIMIZED DIFFUSION IMAGING FOR BRAIN STRUCTURAL CONNECTOME ANALYSIS

BY WILLIAM CONSAGRA^{*} ARUN VENKATARAMAN^{*} AND ZHENGWU ZHANG[†]

University of Rochester^{}, University of North Carolina at Chapel Hill[†]*

High angular resolution diffusion imaging (HARDI), a type of diffusion magnetic resonance imaging (dMRI) that measures diffusion signals on a sphere in q-space, is widely used in data acquisition for human brain structural connectome analysis. Accurate estimation of the local diffusion, and thus the structural connectome, typically requires dense sampling in HARDI, resulting in long acquisition times and logistical challenges. We propose a method to select an optimal set of q-space directions for recovery of the local diffusion under a sparsity constraint on the sampling budget. Relevant historical dMRI data is leveraged to estimate a prior distribution of the local diffusion in a template space using reduced rank Gaussian process models. For a new subject to be scanned, the priors are mapped into the subject-specific coordinate and used to guide an optimized q-space sampling which minimizes the expected integrated squared error of a diffusion function estimator from sparse samples. The optimized sampling locations are inferred by an efficient greedy algorithm with theoretical bounds approximating the global optimum. Simulation studies and a real data application using the Human Connectome Project data demonstrate that our proposed method provides substantial advantages over its competitors.

1. INTRODUCTION. Diffusion Magnetic Resonance Imaging (dMRI) is an advanced MRI methodology that measures the probabilistic motion of water molecules in order to probe tissue microstructure (Stejskal and Tanner, 1965). The earliest applications of dMRI focus on studying the anisotropic diffusion of water in the white matter (WM) using the diffusion tensor imaging (DTI) model (Basser et al., 1994). However, DTI has significant limitations, since it can only describe one major WM fiber direction within each voxel (Tuch et al., 2002), presenting a significant obstacle for efforts to trace WM pathways in crossing fiber regions (Maier-Hein et al., 2017). To overcome this limitation, advanced acquisition methods, such as diffusion spectrum imaging (DSI) (Tuch et al., 2003) and high angular resolution diffusion imaging (HARDI) (Alexander et al., 2002), have been proposed to better characterize the underlying WM structure by estimating an object known as the diffusion orientation distribution function (ODF), denoted here as f . The ODF, or its sharper version, the fiber ODF (fODF) obtained by deconvolving the ODF (Descoteaux et al., 2009), is the primary object of interest for structural connectome mapping. To estimate the structural connectome, tractography algorithms (Tournier et al., 2012; Girard et al., 2014) are applied to the estimated fODF field to compute streamlines connecting different brain regions. Therefore, accurate estimation of the ODF is paramount for performing quality structural connectome analysis.

To estimate the ODF, DSI employs the Fourier relationship between the diffusion ensemble average propagator (EAP), a probability density function characterizing the displacement of water molecule diffusion, and the measured diffusion signal. The ODF can then be calculated from the EAP through radial projection. In HARDI, instead of relying on first computing

Keywords and phrases: diffusion imaging, Gaussian process, experimental design, functional data, structural connectome.

the EAP, the ODF can be directly estimated from the diffusion signal based on the Funk-Radon transform (FRT) (Tuch, 2004). This fact coupled with several other weaknesses of DSI, including the requirement of time-consuming gradient sampling on a three-dimensional Cartesian lattice and large pulsed field gradients to satisfy the Nyquist condition, have contributed to HARDI becoming the more popular dMRI acquisition framework for structural connectome analysis.

Commonly, HARDI data are acquired using uniformly distributed diffusion gradient vectors densely sampled on spheres, known as shells, which inhabit q -space. The distribution of these gradient vectors has been a subject of study, and frequently an electrostatic repulsion model is used to generate their locations (Jones et al., 1999). As shown in this paper, such gradient setting can be sub-optimal with respect to recovering the local diffusion signal. Moreover, in practice, scans are often resource limited and, consequently, parameters are altered for fast data acquisition, e.g., only 15 or less directions are sampled in some studies (Chen et al., 2013; Chang et al., 2015). Therefore, there are two important questions to consider in HARDI: if we are restricted to a limited number of gradient directions to sample, where in q -space should we sample, and given the sparse samples, how do we recover the ODF for connectome analysis? In this paper we address these questions by (a) optimizing the diffusion sampling scheme, and (b) estimating diffusion signal from sparse samples.

The methods proposed in this paper leverage the assumption that high-quality dMRI data are available for the population of interest, e.g. healthy subjects in a certain age range. For simplicity, we only consider diffusion signal on a single shell. The diffusion signal at the v -th voxel can be considered as a realization of a *random function* $X_v \in \mathbb{L}^2(\mathbb{S}^2)$, i.e., a measurable function with realizations in the space of square integrable functions over the 2-sphere. In particular, we assume the distribution of X_v can be modeled as a Gaussian process. Note that Gaussian process models have previously been used to model diffusion signal for applications in image acceleration and motion correction (Andersson and Sotiropoulos, 2015). Employing an empirical Bayesian approach, the historical dMRI data is used to estimate the mean and covariance functions defining X_v , characterizing the prior distribution of the diffusion signal across the brain. This prior is used to derive an estimator for a new subject’s diffusion signal that is robust even in the sparsely sampled case. Additionally, we propose a greedy diffusion direction selection algorithm that sequentially minimizes the voxel-specific mean integrated squared error to direct dMRI data acquisition. In both simulated and real data analyses, the proposed method shows significant advantages over the current dMRI acquisition and signal estimation procedures. In particular, we demonstrate that our method can produce a much better structural connectome reconstruction with sparse diffusion samples.

The incorporation of prior information for the design of q -space sampling sequences has been investigated in the literature. Caruyer and Deriche (2009) propose an optimal sampling scheme in the context of DTI based on minimization of expected squared error of the reconstructed diffusion tensor. Historical data are used to estimate the probability density function of the diffusion tensor field required to calculate the desired expectation. Poot et al. (2010) use diffusion kurtosis imaging (DKI) to form a parametric approximation of the diffusion signal and incorporate a Rician likelihood in order to derive the variance of a parameter of interest as a function of sampling gradient directions. Prior information is incorporated via the DKI parameters estimated from historical subjects, which are then used to approximate the expectation of this quantity by Monte Carlo integration.

Both of the aforementioned methods for q -space optimal design are derived in the context of finite dimensional parametric models for diffusion signal estimation, DTI and DKI, respectively, which can be problematic for connectome analysis, owing to their assumptions of the underlying diffusion process. The proposed modeling framework considers the diffusion signal as a random function with realizations in $\mathbb{L}^2(\mathbb{S}^2)$ and therefore is capable of representing a far richer class of local diffusion patterns than DTI or DKI. Accordingly, the optimal

q-space acquisition problem for the reconstruction of the diffusion signal at a particular voxel is best formulated as a problem of optimal experimental design for the sampling functional data. The application of optimal experimental design techniques to functional data in existing literature is mostly concerned with functions on \mathbb{R} (Ji and Müller, 2017; Wu et al., 2018), though Gao et al. (2018) consider the related problem of landmark selection on arbitrary manifolds. Our approach makes repeated use of the special properties of $\mathbb{L}^2(\mathbb{S}^2)$, especially to incorporate relevant prior information, thus distinguishing our problem from these existing ones. We summarize the main contributions of this work as follows:

1. The diffusion signal is modeled as a random function which allows for more flexibility in the types of signals that can be accommodated than do parametric models such as DTI and DKI. This is particularly important for modeling complex diffusion signals in fiber crossing regions, and faster transformation of the diffusion signal to the ODF. To our knowledge, this is the first work for optimal design in dMRI which both incorporates historical data for constructing priors and does not induce a fixed finite dimensional parametric model for the diffusion signal.
2. In our methodology, we propose to use historical data (e.g., data from large brain imaging studies such as the Human Connectome Project (Glasser et al., 2016)) to construct a spatially varying prior distribution of diffusion signals over all voxels in a template space. These template space priors can easily be ported to the coordinate space of a new subject of interest to facilitate real-time optimal sampling design and sparse sample signal reconstruction, amongst other dMRI tasks of interest.
3. We propose a computationally efficient approximate optimal design algorithm that avoids costly high-dimensional optimization or stochastic techniques such as simulated annealing. Further, we are able to derive computable bounds on the deviation between our approximate solution and the true optimal design.

The rest of the paper is organized as follows. In Section 2, we establish relevant background information from Q-ball imaging, the theory of random functions and Gaussian processes. In Section 3 we present the proposed methodology for addressing optimal sample location selection and diffusion signal reconstruction from sparse samples. Section 4 presents simulation results that compare the performance of our method with one commonly used in the dMRI literature. In Section 5, we show real data examples for several tasks related to dMRI processing and structural connectome analyses. Discussion and future directions are presented in Section 6.

2. BACKGROUND. This section introduces several topics that will be helpful for understanding our methodology development in Section 3, including Q-ball imaging, the theory of random functions, and Gaussian processes.

2.1. Q-ball Imaging for ODF Estimation. Q-ball imaging (Tuch et al., 2003; Tuch, 2004) is a method to reconstruct the ODF describing the underlying WM fiber distribution. Tuch (2004) shows that the ODF can be computed from the diffusion signal on a single sphere in q-space by the Funk-Radon transform (FRT):

$$f(p) = \mathcal{G}(X)(p) = \int_{r \in \mathbb{S}^2} \delta(r^\top p) X(r) dr$$

where $p \in \mathbb{S}^2$, f is the ODF, \mathcal{G} represents the FRT, X represents the true diffusion function on \mathbb{S}^2 , and δ is the Dirac delta function. Q-ball imaging provides an advancement over previous models for structural connectome mapping due to the fact that: 1) diffusion signals need only to be measured on a single sphere in q-space, and thus far fewer acquisitions are required

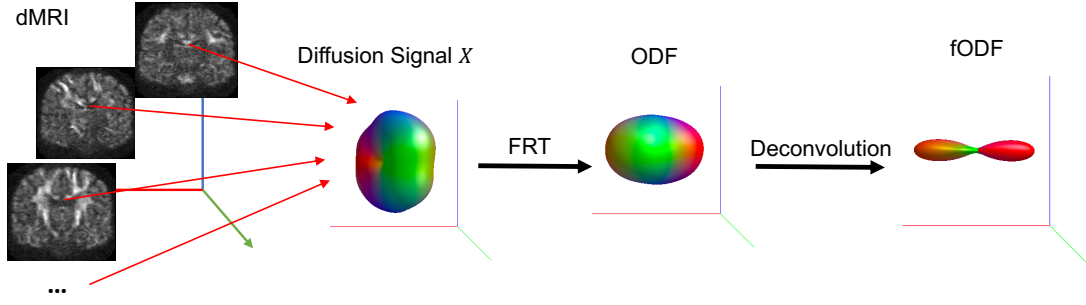


Fig 1: Illustration of the process of constructing fODF from dMRI measures. Discrete dMRI measures along different b-vectors are used to estimate a smoothed diffusion signal X , which is then transformed into the ODF function and then fODF for structural connectome analysis.

compared with DSI; 2) it is model-independent and does not require the Gaussian assumption present in many models, which often is violated in practice (Tuch et al., 2002); 3) the ODF gives a much higher resolution representation of the fiber profile than the diffusion tensor (DTI); 4) a convenient spherical deconvolution can be applied to the ODF to get the sharper fODF that better reflects the fiber configuration in a voxel (Descoteaux et al., 2009); and 5) there are analytical forms to translate the diffusion signal X to the ODF f and further to fODF, under certain basis system (Descoteaux et al., 2007). Figure 1 illustrates the process of constructing a smoothed diffusion signal X , ODF and fODF from discrete dMRI measures.

There are two popular methods to estimate a continuous signal on \mathbb{S}^2 from discrete dMRI observations: 1) the kernel smoothing method presented in Tuch (2004), and 2) the penalized regression method presented in Descoteaux et al. (2007). However, both of these techniques use data from only one voxel in one subject and do not allow for the incorporation of valuable prior information gleaned from readily available high-resolution data. If the diffusion resolution (number of b-vectors) is low, such estimation will be problematic, which motivates our development of alternative procedures.

2.2. Random Functions and Gaussian Processes. Let \mathcal{D} be a compact subset of \mathbb{R}^d , in this application $\mathcal{D} = \mathbb{S}^2$. Consider the function space $\mathbb{L}^2(\mathcal{D}) = \{X : \mathcal{D} \rightarrow \mathbb{R} : \int_{\mathcal{D}} X^2(p) d\lambda(p) < \infty\}$, the collection of square integrable functions with respect to measure λ over \mathcal{D} . This is a Hilbert space with inner product defined by $\langle X, Y \rangle_{\mathbb{L}^2(\mathcal{D})} = \int_{\mathcal{D}} X(p)Y(p) d\lambda(p)$ for $X, Y \in \mathbb{L}^2(\mathcal{D})$. With slight abuse of notation, let X be a random function defined on probability space (Ω, \mathcal{F}, P) with realizations in $\mathbb{L}^2(\mathcal{D})$, i.e., X is a measurable function from $\Omega \rightarrow \mathbb{L}^2(\mathcal{D})$. Define $\mathbb{E}_P[X] = \mu$ and covariance function $C = \mathbb{E}_P[(X - \mu)(X - \mu)]$ and assume that $\int_{\mathcal{D}} \int_{\mathcal{D}} C^2(p, t) d\lambda(p) d\lambda(t) < \infty$. By Mercer's theorem, the covariance function is guaranteed the eigen-decomposition $C(p, t) = \sum_{k=1}^{\infty} \rho_k \psi_k(p) \psi_k(t)$, where $\{\psi_k\}_{k=1}^{\infty}$ forms an orthonormal sequence of eigenfunctions in $\mathbb{L}^2(\mathcal{D})$ and $\{\rho_k\}_{k=1}^{\infty}$ is a non-increasing sequence of real, non-negative eigenvalues. The spectral data of C is defined by the infinite dimensional integral equation

$$(1) \quad \int_{\mathcal{D}} C(p, t) \psi_k(t) d\lambda(t) = \rho_k \psi_k(p) \text{ for } k = 1, 2, \dots, \infty,$$

with orthogonality constraint $\int_{\mathcal{D}} \psi_k(p) \psi_j(p) = \delta_{kj}$, where δ_{kj} is the Kronecker delta function (Hsing and Eubank, 2013). The eigenfunctions can also be used to form a useful decomposition of the random function X . By the Karhunen-Lo  ve theorem (Karhunen, 1946), with probability one we have

$$(2) \quad X(p) = \mu(p) + \sum_{k=1}^{\infty} \xi_k \psi_k(p),$$

where $\xi_k = \langle X - \mu, \psi_k \rangle_{\mathbb{L}^2(\mathcal{D})}$, which are mean zero random variables with $\mathbb{E}_P[\xi_k \xi_j] = \rho_k \delta_{kj}$. The convergence of the sum in Equation (2) holds uniformly since $\sup_{p \in \mathcal{D}} \mathbb{E}_P[(X(p) - \mu(p) - \sum_{k=1}^K \xi_k \psi_k(p))^2] \rightarrow 0$ as $K \rightarrow \infty$. The expansion in Equation (2) also facilitates parsimonious representation as the first K eigenfunctions form the best rank- K basis system for representing X , in terms of minimum expected mean integrated squared error (MISE). That is, if $\{e_k\}_{k=1}^{\infty}$ is a complete orthogonal basis system for $\mathbb{L}^2(\mathcal{D})$, then $\mathbb{E}_P[\|X - \mu - \sum_{k=1}^K \langle X, e_k \rangle_{\mathbb{L}^2(\mathcal{D})} e_k\|_{\mathbb{L}^2(\mathcal{D})}^2]$ is minimized by taking $e_k = \psi_k$ for $k = 1, 2, \dots, K$.

Functional data typically comes in the form of a sample $\{X_1, \dots, X_N\}$ of independent realizations of X , where the i^{th} realization is observed at a discrete set of points $p_{i1}, \dots, p_{iM_i} \in \mathcal{D}$. In this work, each $X_i(p_{im})$ is assumed to be contaminated with independent additive error ϵ_{im} with mean 0 and variance σ_i^2 , i.e., the observed signal is modeled as

$$(3) \quad S_i(p_{im}) = X_i(p_{im}) + \epsilon_{im} \text{ for } i = 1, \dots, N, \text{ and } m = 1, \dots, M_i.$$

The technique of functional principal component analysis (FPCA) refers to methods for estimating the eigenfunctions and eigenvalues from the observed data $\{S_i(p_{im})\}$. FPCA is often done in an exploratory context, where the first few eigenfunctions are used to analyze the dominant modes of variation of a function sample. In this work, we use the FPCA in order to construct an optimal parsimonious basis for subsequent estimation of functional samples when only discrete and sparse data points are observed.

An important and widely used class of random function is the so-called Gaussian process, abbreviated GP from here on. A GP on \mathcal{D} is defined as a stochastic process such that for any finite collection of points $p_1, p_2, \dots, p_M \in \mathcal{D}$ the joint distribution of the process at these locations is a multivariate Gaussian with mean $(\mu(p_1), \mu(p_2), \dots, \mu(p_M))^{\top} \in \mathbb{R}^M$ and covariance matrix $\mathbf{C}_M \in \mathbb{R}^{M \times M}$ such that $[\mathbf{C}_M]_{ij} = C(p_i, p_j)$, and is denoted as $\text{GP}(\mu, C)$. It is easy to show that a random function X with the decomposition (2) is a GP if and only if ξ_k are normally distributed, i.e., $\xi_k \sim \mathcal{N}(0, \rho_k)$. We will see there are situations where it is convenient or necessary to use GP models that are degenerate, i.e., whose covariance functions have only finitely many non-zero eigenvalues. In this case, a valid GP may still be constructed by assuming a Gaussian distribution on ξ_k for $k = 1, 2, \dots, K$. Such a formulation has been termed a *reduced rank GP*, and Qui  nero-Candela and Rasmussen (2005) offer an extensive treatment of its properties.

3. METHODS. The observed diffusion signal, normalized with respect to the mean non diffusion-weighted signal (diffusion signal at b-value equal to 0), at voxel $v \in \mathcal{V}_i$ for subject i is denoted as $\{S_{vi}(p_{i1}), \dots, S_{vi}(p_{iM_i})\}$, where $p_{im} \in \mathbb{S}^2$ represents one of the M_i diffusion gradient directions (i.e., b-vectors in dMRI), and \mathcal{V}_i represents the set of voxels in a region of interest (e.g., voxels in the white matter of subject i). For notational simplicity, from here on we will denote $S_{vi}(p_{im})$ as s_{vim} . We assume that all of the M_i directions correspond to the same shell, e.g., with b-value equal to 1000. We also assume the statistical model (3) at each voxel: $s_{vim} = X_{vi}(p_{im}) + \epsilon_{vim}$, where $X_{vi} \in \mathbb{L}^2(\mathbb{S}^2)$ is the true diffusion signal for subject

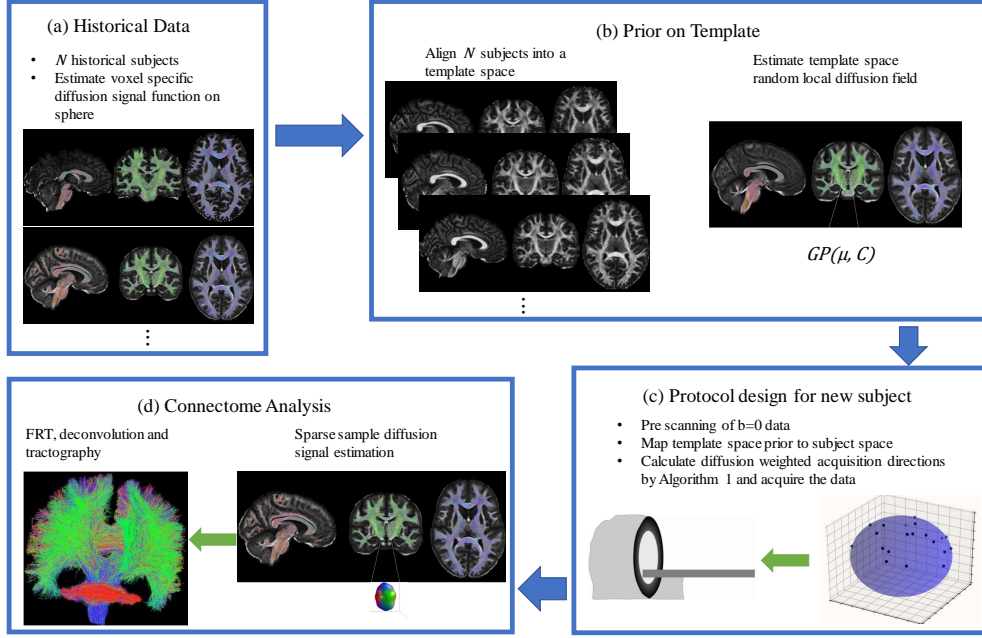


Fig 2: Flowchart of the proposed methodology: (a) estimation of historical diffusion signal, (b) construction of template space prior, (c) mapping template space prior to subject space for diffusion direction selection and (d) downstream dMRI analysis tasks, e.g. connectome analysis.

i at voxel v and is a realization of a voxel specific Gaussian process and $\epsilon_{vim} \sim \mathcal{N}(0, \sigma_i^2)$, which is independent of the diffusion direction p_{im} and brain region v .

We further assume that we have access to a relevant collection of high-resolution historical dMRI data, denoted as $\mathcal{H} = \{(p_{im}, s_{vim}) : \text{for } m = 1, \dots, M_i \text{ and } i = 1, \dots, N \text{ and } v = 1, \dots, |\mathcal{V}_i|\}$, where N represents the number of subjects. Such data are ubiquitous and easy to access due to recent efforts from the HCP and the UK Biobank. We would like to leverage \mathcal{H} to build priors over the diffusion signals and then use them to guide both dMRI acquisition and signal reconstruction for new subjects. This proves challenging in that each subject's data in \mathcal{H} is gathered in a different coordinate system, referred to here as the subject space, and moreover, the subjects have different brain morphology. We circumvent this issue by performing a registration of each of the historical subjects to a common space, referred to here as the template space. A GP model for the distribution of diffusion signal at each voxel in the template space is estimated from the aligned data. The warping function used to perform registration is constrained to be a diffeomorphism. As a result, for any subject of interest that has been registered to the template space, the inverse warping can be used to map the estimated priors from the template space to the subject space smoothly to guide our analysis. This pipeline is illustrated in Figure 2 and described in detail over the remainder of the section.

3.1. Prior Summarization From Historical Data.

3.1.1. Diffusion Signal Estimation in Subject Space. Given the fact that data in \mathcal{H} are acquired with high-resolution, we can confidently estimate smoothed diffusion signal functions at each voxel independently. Following the procedure in Descoteaux et al. (2007), we

model the diffusion signal as a linear combination of elements from an orthonormal basis system for symmetric functions in $\mathbb{L}^2(\mathbb{S}^2)$ constructed from the spherical harmonics, denoted as $\{\phi_j\}_{j=1}^J$. The coefficients of the expansion are estimated by regularized least squares regression with a second order roughness penalty. That is, for voxel v in subject i , its diffusion signal can be estimated by solving the following regularized least squares problem

$$\hat{\mathbf{c}}_{vi} = \operatorname{argmin}_{\mathbf{c} \in \mathbb{R}^J} \sum_{m=1}^{M_i} (s_{vim} - \mathbf{c}^\top \phi(p_{im}))^2 + \lambda_i \int_{\mathbb{S}^2} (\Delta_{\mathbb{S}^2}(\mathbf{c}^\top \phi(p)))^2 dp,$$

where $\phi(p) = (\phi_1(p), \dots, \phi_J(p))^\top$, $\Delta_{\mathbb{S}^2}$ denotes the Laplace-Beltrami operator on \mathbb{S}^2 and penalty $\lambda_i > 0$ is selected by minimizing the generalized cross validation (GCV) criteria. The resulting smoothed estimate of diffusion signal is given by $\hat{X}_{vi}(p) = \hat{\mathbf{c}}_{vi}^\top \phi(p)$. More details on this estimation procedure can be found in the supplementary materials.

3.1.2. Mean and Covariance in Template Space. Let γ_i be the diffeomorphic warping function from the historical subject i to the template space based on the subject's diffusion data (e.g., fractional anisotropy or FA image) (Avants et al., 2008). The warping function deforms the regular voxel grid in subject space to align the subject's data to the template, and a re-gridding procedure is needed in the template space to reconstruct a regular voxel grid for the subject. We can obtain an estimate of the subject's diffusion function at each of the voxels in the template space through interpolation of \hat{X}_{vi} . That is, for any voxel \tilde{v} in the template space, we have $\hat{X}_{\tilde{v}i}(p) = \hat{\mathbf{c}}_{\tilde{v}i}^\top \phi(p)$ where $\hat{\mathbf{c}}_{\tilde{v}i}$ is computed by a linear interpolation scheme applied to $\{\hat{\mathbf{c}}_{vi}\}$ for v 's in the subject space mapped near \tilde{v} by γ_i . We use the popular Advanced Normalization Tools (ANTs) to perform this alignment and refer the reader to Avants et al. (2009) for more details on the interpolation procedure.

Once the aligned diffusion signal $\hat{X}_{\tilde{v}i}(p)$ has been computed for all subject in \mathcal{H} , the mean and covariance functions at \tilde{v} can be estimated by the following empirical estimators

$$(4) \quad \hat{\mu}_{\tilde{v}}(p) = \hat{\mathbf{c}}_{\tilde{v}}^\top \phi(p),$$

$$(5) \quad \hat{C}_{\tilde{v}}(p, t) = \phi(p)^\top \hat{\Sigma}_{\tilde{v}} \phi(t)$$

where $\hat{\mathbf{c}}_{\tilde{v}}$ and $\hat{\Sigma}_{\tilde{v}}$ are the sample mean and covariance matrix of $\{\hat{\mathbf{c}}_{\tilde{v}1}, \dots, \hat{\mathbf{c}}_{\tilde{v}N}\}$, respectively. We assume a large historical sample, $N \gg J$ and therefore we expect these estimators to be stable. Then for each \tilde{v} , the distribution of the diffusion signal on \mathbb{S}^2 is modeled by the reduced rank GP($\hat{\mathbf{c}}_{\tilde{v}}^\top \phi$, $\phi^\top \hat{\Sigma}_{\tilde{v}} \phi$).

3.1.3. Mean and Covariance in Subject Space. Let γ be the template space warping function for a subject of interest, who may or may not be in \mathcal{H} . We want to map the GP priors from the template to this subject space for future diffusion data analysis, such as constructing an optimal diffusion sampling scheme and subsequent diffusion signal function estimation. To do this, we map the template space mean and covariance functions to the subject space and use them to define a GP adapted to the subject space coordinate system. The mean functions are identified as a vector in \mathbb{R}^J , and therefore the same linear interpolation scheme we use to warp the estimated historical diffusion functions from Section 3.1.2 can be used for estimating $\hat{\mu}_v$ in the subject space. On the other hand, the covariance functions are identified by symmetric positive definite (SPD) matrices $\hat{\Sigma}_{\tilde{v}}$ and thus the estimate of the covariance function \hat{C}_v for subject space voxel v requires an interpolation of SPD matrices. Considering the non-Euclidean structure of the SPD matrix manifold, we propose the following interpolation scheme.

Denote \mathcal{S}_+^J the manifold of $J \times J$ SPD matrices and let M_1, \dots, M_n be a sample of SPD matrices. The weighted Karcher mean of the sample is defined as

$$(6) \quad M_{Kmean} = \operatorname{argmin}_{M \in \mathcal{S}_+^J} \sum_{i=1}^n w_i d^2(M_i, M), \text{ with } \sum_{i=1}^n w_i = 1,$$

where $d(\cdot, \cdot)$ is induced by a selected Riemannian metric. If we let the weights w_i be proportional to the Euclidean distance between $\gamma^{-1}(\tilde{v}_i)$ and the voxel of interest v in the subject space, the weighted Karcher mean can be used as an interpolation scheme of the covariance functions.

There are several valid metrics that can be chosen to compute the distance between elements in \mathcal{S}_+^J (Arsigny et al., 2007). It is easy to show $\int_{\mathbb{S}^2 \times \mathbb{S}^2} (\hat{C}_{\tilde{v}_1}(p, t) - \hat{C}_{\tilde{v}_2}(p, t))^2 dp dt = \|\hat{\Sigma}_{\tilde{v}_1} - \hat{\Sigma}_{\tilde{v}_2}\|_F^2$, so using the standard Euclidean (Frobenius) norm as a metric for the interpolation appears as a reasonable choice. However, interpolation of SPD matrices under the Euclidean norm can result in a “swelling” effect, in which the determinant of the interpolated value is larger than the determinant of any of the original SPD matrices (Dryden et al., 2009). This would result in an undesirable amplification of the estimated variability. To overcome this limitation, we use the log-Euclidean metric proposed in Arsigny et al. (2007) to perform the interpolation (6), defined as

$$\|M_1 - M_2\|_{Log}^2 = \|\log(M_1) - \log(M_2)\|_F^2,$$

where $\log(\cdot)$ represents the matrix logarithm. For any $M \in \mathcal{S}_+^J$, the matrix logarithm always exists and is defined by $\log(M) = V \log(D) V^\top$, where V is the matrix whose columns are the eigenvectors of M and D is the diagonal matrix of eigenvalues. Since D is diagonal, the matrix logarithm has an especially simple form: $\log(D) = \text{Diag}(\log(D_{11}), \log(D_{22}), \dots, \log(D_{JJ}))$. The subject space covariance function for voxel v is defined by the solution to the interpolation (6) applied to the set of $\hat{\Sigma}_{\tilde{v}}$, for \tilde{v} mapped near v by γ^{-1} , with $d(M_1, M_2) = \|M_1 - M_2\|_{Log}^2$.

3.2. Diffusion Signal Estimation from Sparse Samples. Our main goal is to develop an optimized gradient table to sample the diffusion signal when only a few diffusion directions can be reliably measured. The optimization will depend on the choice of estimator for the diffusion signal function, which must be adapted to the situation of sparsely sampled data. We propose our estimator in this section and develop the optimized sampling scheme in the section that follows. Note, since the estimation is performed at the voxel level, in what follows we suppress the subscript v for notational simplicity.

The true diffusion function at a voxel is assumed to be a realization of the voxel specific random function $X \sim \text{GP}(\mu, C)$. We consider the estimation of the diffusion signal function for sparsely sampled dMRI, i.e., $\{(p_m, s_m)\}_{m=1}^M$ with a small M . To facilitate future connectome extraction, it is important to obtain a continuous representation of the estimated diffusion function with respect to basis functions $\{\phi_1, \dots, \phi_J\}$, since with such a representation there is a closed form transformation from diffusion signal function to ODF for fiber tracking via the FRT (Descoteaux et al., 2007). However, direct estimation the coefficient of ϕ_j with sparse and irregular observations can be problematic, as illustrated in James et al. (2000), where a reduced rank solution was promoted. As outlined in Section 2, the optimal rank K basis system for representing X in terms of minimum expected integrated squared error is given by the first K eigenfunctions of the covariance function C , denoted as $\{\psi_1, \dots, \psi_K\}$. Due to this optimality property we adopt the $\{\psi_1, \dots, \psi_K\}$ for sparse sample modeling. If we impose the restriction that ψ_k lies in the linear span of $\{\phi_1, \dots, \phi_J\}$, then there exists a simple linear transformation between the ψ_k ’s and ϕ_j ’s, and thus we can still leverage the analytic

FRT for sparse sample ODF estimation. Furthermore, this restriction translates the infinite dimensional integral Equation (1) to the following finite dimensional eigenvalue problem:

$$\hat{\Sigma} \hat{\mathbf{b}}_k = \hat{\rho}_k \hat{\mathbf{b}}_k, \text{ for } k = 1, 2, \dots, J,$$

with orthonormality restriction

$$\hat{\mathbf{b}}_i^\top \hat{\mathbf{b}}_j = \begin{cases} 1 & i = j \\ 0 & i \neq j \end{cases},$$

i.e. FPCA applied to the subject space covariance function C . The estimate of the k -th eigenfunction is given by $\hat{\psi}_k(p) = \hat{\mathbf{b}}_k^\top \phi(p)$, with the corresponding eigenvalue $\hat{\rho}_k$. The rank of the model K ($K \leq J$) can be chosen based on a threshold of the proportion of variance explained (PVE) or by using an information criteria.

Given the sparse sample $\{(p_m, s_m)\}$ and historical data \mathcal{H} , we would like to obtain an estimate of X in the form $X(p) = \mu(p) + \sum_{k=1}^K \xi_k \psi_k(p)$. An estimate of ξ_k can be constructed by computing the conditional distribution of $P(\xi_K | s_M, \mathbf{P}_M, \mathcal{H})$, where $\xi_K = (\xi_1, \dots, \xi_K)^\top$, $s_M = (s_1, \dots, s_M)^\top$ and $\mathbf{P}_M = (p_1, \dots, p_M)^\top$. We suppress $(\mathbf{P}_M, \mathcal{H})$ in the following conditioning notations since all of them are conditional on $(\mathbf{P}_M, \mathcal{H})$. Given the model (3) and Gaussian assumptions, we can easily derive the following joint distribution on (ξ_K, s_M)

$$(\xi_K, s_M)^\top \sim \mathcal{N} \left((\mathbf{0}_K, \mu_M)^\top, \begin{bmatrix} \mathbf{\Lambda}_K & \mathbf{\Lambda}_K \mathbf{\Psi}_{M,K}^\top \\ \mathbf{\Psi}_{M,K} \mathbf{\Lambda}_K & \mathbf{\Psi}_{M,K} \mathbf{\Lambda}_K \mathbf{\Psi}_{M,K}^\top + \sigma^2 \mathbf{I}_M \end{bmatrix} \right),$$

where $\mu_M = (\mu(p_1), \dots, \mu(p_M))^\top$, $\mathbf{\Lambda}_K = \text{Diag}(\rho_1, \dots, \rho_K)$, and $\mathbf{\Psi}_{M,K} \in \mathbb{R}^{M \times K}$ such that $[\mathbf{\Psi}_{M,K}]_{mk} = \psi_k(p_m)$ for $m = 1, \dots, M$ and $k = 1, \dots, K$. Therefore, $P(\xi_K | s_M)$ is a normal distribution (Mardia et al. (1979), Theorem 3.2.4) with mean,

$$(7) \quad \mathbb{E}[\xi_K | s_M] = \mathbf{\Lambda}_K \mathbf{\Psi}_{M,K}^\top [\mathbf{\Psi}_{M,K} \mathbf{\Lambda}_K \mathbf{\Psi}_{M,K}^\top + \sigma^2 \mathbf{I}_M]^{-1} (s_M - \mu_M).$$

Based on $\mathbb{E}[\xi_K | s_M]$, we propose the following estimator of X :

$$(8) \quad \begin{aligned} \tilde{X} &= \mathbb{E}[X(p) | s_M] = \mu(p) + \psi_K(p)^\top \mathbb{E}[\xi_K | s_M] \\ &= \mu(p) + \psi_K(p)^\top \mathbf{\Lambda}_K \mathbf{\Psi}_{M,K}^\top [\mathbf{\Psi}_{M,K} \mathbf{\Lambda}_K \mathbf{\Psi}_{M,K}^\top + \sigma^2 \mathbf{I}_M]^{-1} (s_M - \mu_M) \end{aligned}$$

where $\psi_K(p) = (\psi_1(p), \dots, \psi_K(p))^\top$ and \mathbf{I}_M is the $M \times M$ identity matrix.

Yao et al. (2005) use the estimator (8) for the case of sparsely observed longitudinal data on \mathbb{R} . It is notable that (7) is both the best estimate of the coefficients under the Gaussian assumption and the best linear predictor even when the Gaussian assumption is violated. In theory, this provides robustness to some deviations from the Gaussian assumption, a property that will be verified in simulations in Section 4. Alternatively, the derivation above can be motivated through a fully Bayesian framework under the prior that $X \sim \text{GP}(\mu, C)$, or equivalently $\xi_K \sim \mathcal{N}(0, \mathbf{\Lambda}_K)$, where it can be shown that the mean of the posterior predictive distribution for $X(p)$ is exactly (8) (see the supplemental material for more details).

To obtain \tilde{X} , the parameters μ , ψ_K , $\mathbf{\Lambda}_K$, $\mathbf{\Psi}_{M,K}$ and K are estimated from \mathcal{H} . Moreover, σ^2 , the measurement error variance for the current subject, also plays an important role in estimating X . It is important to estimate σ^2 from the new subject's data instead of estimating it from \mathcal{H} , since the scanner used for collecting the subject's data may be different from the scanner used to collect the historical data. We propose a simple estimation based on the subject's $b = 0$ (non-diffusion weighted) data with the assumption that we have access to n (> 2) $b = 0$ images for the subject of interest, e.g. collected at some pre-screening. See the supplemental material for further elaboration and evaluation of this estimator.

3.3. Optimal q-Space Sampling. Given the estimator (8), we formulate the diffusion sampling, the process of obtaining \mathbf{s}_M in q-space, as an optimization problem: for a fixed total budget of M samples, our goal is to select a set of directions $\mathbf{P}_M = (p_1, \dots, p_M)^\top$ such that the expected integrated squared error of the estimated diffusion signal, conditional on \mathbf{P}_M , is minimized. Denote the optimal locations as \mathbf{P}_M^* , which will be referred to as the optimal q-space design. We first consider this problem for a single voxel and then extend it to a set of voxels in a region of interest.

3.3.1. Optimal Diffusion Sampling for One Voxel. At a particular voxel, we identify the optimal q-space design as the solution to the following optimization problem:

$$(9) \quad \mathbf{P}_M^* = \underset{\mathbf{P}_M \in \times_{m=1}^M \mathbb{S}^2}{\operatorname{argmin}} \mathbb{E} \left(\int_{\mathbb{S}^2} \left(X(p) - \tilde{X}(p) \right)^2 dp \right),$$

where \tilde{X} is the estimator from Equation (8) which relies on \mathbf{P}_M , and the expectation is with respect to the distribution of X at this voxel. Expanding the square and swapping the integral and the expectation operators, it is straightforward to show that (9) can be equivalently formulated as the following maximization problem:

$$(10) \quad \mathbf{P}_M^* = \underset{\mathbf{P}_M \in \times_{m=1}^M \mathbb{S}^2}{\operatorname{argmax}} \int_{\mathbb{S}^2} \mathbf{c}_M(p)^\top \mathbf{\Gamma}_M^{-1} \mathbf{c}_M(p) dp.$$

where, under the rank K assumption on C , we have $\mathbf{c}_M(p) = \mathbf{\Psi}_{M,K} \mathbf{\Lambda}_K \psi_K(p)$ and $\mathbf{\Gamma}_M = \mathbf{\Psi}_{M,K} \mathbf{\Lambda}_K \mathbf{\Psi}_{M,K}^\top + \sigma^2 \mathbf{I}_M$. Substituting these definitions into (10) and integrating, we arrive at the following finite dimensional optimization problem:

$$(11) \quad \mathbf{P}_M^* = \underset{\mathbf{P}_M \in \times_{m=1}^M \mathbb{S}^2}{\operatorname{argmax}} \operatorname{trace}(\mathbf{\Lambda}_K \mathbf{\Psi}_{M,K}^\top \mathbf{\Gamma}_M^{-1} \mathbf{\Psi}_{M,K} \mathbf{\Lambda}_K).$$

In practice, it is often sufficient to constrain the candidate design points to be in a large but finite set $\mathcal{A} \subset \mathbb{S}^2$, e.g. a dense equispaced grid on \mathbb{S}^2 to measure diffusion-weighted signals. In this scenario, the problem (11) can be written as

$$(12) \quad \mathbf{P}_M^* = \underset{\mathbf{P}_M \in \mathcal{P}_M(\mathcal{A})}{\operatorname{argmax}} g(\mathbf{P}_M),$$

where $\mathcal{P}_M(\mathcal{A}) = \{(p_1, \dots, p_M)^\top : p_i \in \mathcal{A}\}$ and

$$g(\mathbf{P}_M) = \operatorname{trace}(\mathbf{\Lambda}_K \mathbf{\Psi}_{M,K}^\top \mathbf{\Gamma}_M^{-1} \mathbf{\Psi}_{M,K} \mathbf{\Lambda}_K).$$

The global problem (12) is an integer program and is known to be NP-hard. To circumvent this computational bottleneck, we propose a sequential search strategy for producing a greedy approximation $\hat{\mathbf{P}}_M^* = (\hat{p}_1, \dots, \hat{p}_M)^\top$. Assuming that we have selected $\hat{p}_1^*, \dots, \hat{p}_{m-1}^*$ in the previous rounds, we propose solving the conditional optimization problem to obtain \hat{p}_m^* ,

$$(13) \quad \hat{p}_m^* = \underset{p_m \in \mathcal{A}}{\operatorname{argmax}} \operatorname{trace}(\mathbf{\Lambda}_K \mathbf{\Psi}_{m,K}^\top \mathbf{\Gamma}_m^{-1} \mathbf{\Psi}_{m,K} \mathbf{\Lambda}_K),$$

where $\mathbf{\Psi}_{m,K} \in \mathbb{R}^{m \times K}$ is the eigenfunction evaluation matrix over $(\hat{p}_1^*, \dots, \hat{p}_{m-1}^*, p_m)$ and $\mathbf{\Gamma}_m = \mathbf{\Psi}_{m,K} \mathbf{\Lambda}_K \mathbf{\Psi}_{m,K}^\top + \sigma^2 \mathbf{I}_m$.

Algorithm 1 presents an efficient procedure for sequentially solving (13) by making use of a rank one update scheme to compute $\mathbf{\Gamma}_m^{-1}$ that leverages the block matrix inversion formula

to avoid a series of costly matrix inversions, especially when m gets large. Specifically, it is easy to see that $\mathbf{\Gamma}_m$ can be partitioned as

$$\mathbf{\Gamma}_m = \begin{pmatrix} \mathbf{\Gamma}_{m-1} & \mathbf{h} \\ \mathbf{h}^\top & q \end{pmatrix},$$

where $\mathbf{h} = \mathbf{\Psi}_{m-1,K} \mathbf{\Lambda}_K \boldsymbol{\psi}_K(p_m) \in \mathbb{R}^{m-1}$ and $q = \boldsymbol{\psi}_K(p_m)^\top \mathbf{\Lambda}_K \boldsymbol{\psi}_K(p_m) + \sigma^2 \in \mathbb{R}$ with $\boldsymbol{\psi}_K(p_m) = (\psi_1(p_m), \dots, \psi_K(p_m))^\top$, and p_m is a candidate point in \mathcal{A} for \hat{p}_m^* . As a result, the inverse of $\mathbf{\Gamma}_m$ can be computed efficiently through

$$(14) \quad \mathbf{\Gamma}_m^{-1} = \begin{pmatrix} \mathbf{\Gamma}_{m-1}^{-1}(\mathbf{I}_{m-1} + a\mathbf{h}\mathbf{h}^\top\mathbf{\Gamma}_{m-1}^{-1}) - a\mathbf{\Gamma}_{m-1}^{-1}\mathbf{h} \\ -a\mathbf{h}^\top\mathbf{\Gamma}_{m-1}^{-1} & a \end{pmatrix},$$

where $a = (q - \mathbf{h}^\top \mathbf{\Gamma}_{m-1}^{-1} \mathbf{h})^{-1} \in \mathbb{R}$, and $\mathbf{\Gamma}_{m-1}^{-1}$ is precomputed based on the iteration of finding \hat{p}_{m-1} .

A question that naturally arises is: how good is the approximation $\hat{\mathbf{P}}_M^*$? In Theorem 1, we provide a bound for the ratio of the performance between the greedy approximation from Algorithm 1 and the global optimum from (12).

THEOREM 1. *Let $\hat{\mathbf{P}}_m^*$ be the approximate design obtained after m iterations of Algorithm 1. Define $\lambda_\psi^* = \max_{p \in \mathcal{A}} \lambda_{\max}(\boldsymbol{\psi}_K(p) \boldsymbol{\psi}_K(p)^\top)$, where λ_{\max} is the function which returns the maximum eigenvalue of its argument. Then*

$$(15) \quad g(\hat{\mathbf{P}}_m^*) \geq \left[1 - \exp\left(\frac{-1/\rho_1}{1/\rho_K + \frac{m}{\sigma^2} \lambda_\psi^*} \frac{m}{M}\right) \right] g(\mathbf{P}_M^*)$$

where \mathbf{P}_M^* is the solution to (12).

For a proof of Theorem 1 and an interpretation of (15) in terms of the distribution of the random function X , see the supplemental material.

Algorithm 1 Algorithm for greedy approximation to (9)

- 1: **Input:** Diagonal matrix of eigenvalues $\mathbf{\Lambda}_K$, eigenfunctions $\{\psi_1, \dots, \psi_K\}$, possible design points \mathcal{A} , measurement error variance σ^2 , and total budget $M \in \mathbb{N}$.
 - 2: **Output:** Vector of indices defining the design \mathbf{i}
 - 3: **Initialize:** $\mathbf{i} \leftarrow \text{zeros}(M)$, list of indices of $\mathbf{a} = (1, 2, \dots, |\mathcal{A}|)$
 - 4: **for** $m = 1 : M$ **do**
 - 5: $v_{\text{optim}} \leftarrow 0$
 - 6: **for** n in \mathbf{a} **do**
 - 7: $\boldsymbol{\psi}_n \leftarrow (\psi_1(p_n), \dots, \psi_K(p_n))^\top$ for $p_n \in \mathcal{A}$
 - 8: **if** $m = 1$ **then** \triangleright handle boundary case
 - 9: $\boldsymbol{\Psi}_n \leftarrow \boldsymbol{\psi}_n^\top$; $\mathbf{\Gamma}_n^{-1} \leftarrow [\boldsymbol{\Psi}_n \mathbf{\Lambda}_K \boldsymbol{\Psi}_n^\top + \sigma^2]^{-1}$
 - 10: **else**
 - 11: compute $\mathbf{\Gamma}_n^{-1}$ using formula (14) and let $\boldsymbol{\Psi}_n \leftarrow (\boldsymbol{\Psi}_{m-1,K}, \boldsymbol{\psi}_n^\top)^\top$
 - 12: $v_n \leftarrow \text{trace}(\mathbf{\Lambda}_K \boldsymbol{\Psi}_n^\top \mathbf{\Gamma}_n^{-1} \boldsymbol{\Psi}_n \mathbf{\Lambda}_K)$
 - 13: **if** $v_n > v_{\text{optim}}$ **then**
 - 14: $i_{\text{optim}} \leftarrow n$; $v_{\text{optim}} \leftarrow v_n$; $\tilde{\boldsymbol{\Psi}}_{\text{optim}} \leftarrow \tilde{\boldsymbol{\Psi}}_n$; $\mathbf{\Gamma}_{\text{optim}}^{-1} \leftarrow \mathbf{\Gamma}_n^{-1}$
 - 15: $\mathbf{i}(m) \leftarrow i_{\text{optim}}$ and remove $\mathbf{i}(m)$ from \mathbf{a}
 - 16: $\boldsymbol{\Psi}_m \leftarrow \tilde{\boldsymbol{\Psi}}_{\text{optim}}$; $\mathbf{\Gamma}_m^{-1} \leftarrow \mathbf{\Gamma}_{\text{optim}}^{-1}$
-

3.3.2. Extension to Multiple Voxels. The previous formulation considers the optimal design for recovery of the diffusion signal function for a single voxel. We now discuss how to extend our construction to the case when a single q-space design is needed for a collection of voxels in a region of interest \mathcal{V}_s . When $\mathcal{V}_s = \mathcal{V}$, we can create an acquisition scheme that jointly optimizes over the whole WM, and when \mathcal{V}_s corresponds to voxels covering certain fiber bundles, we can construct an optimal sampling scheme to accurately recover these fiber bundles. In any case, extending the objective function in (9) to perform joint optimization $\forall v \in \mathcal{V}_s$ may be accommodated by minimizing the sum over the region

$$\sum_{v \in \mathcal{V}_s} w_v \mathbb{E} \left(\int_{\mathbb{S}^2} (X_v(p) - \tilde{X}_v(p))^2 dp \right), \text{ with } \sum_{v \in \mathcal{V}_s} w_v = 1.$$

If no a-priori weighting is assumed, we can let $w_v = |\mathcal{V}_s|^{-1}$, and by similar derivations as in Section 3.3.1, the sequential optimization problem in (13) now becomes

$$(16) \quad \hat{p}_m^* = \operatorname{argmax}_{p_m \in \mathcal{A}} \sum_{v \in \mathcal{V}_s} \operatorname{trace} \left(\Lambda_K^{(v)} \Psi_{m,K}^{(v) \top} [\Psi_{m,K}^{(v)} \Lambda_K^{(v)} \Psi_{m,K}^{(v) \top} + \sigma^2 \mathbf{I}_m]^{-1} \Psi_{m,K}^{(v)} \Lambda_K^{(v)} \right),$$

where the superscript v indicates the voxel specific data. Simple augmentation of Algorithm 1 can be made to accommodate this situation.

4. SIMULATION STUDY. We compared the proposed diffusion signal sampling and fitting scheme with a commonly used sampling approach called the electrostatic repulsion model (ESR) (Jones et al., 1999) and signal fitting by regularized spherical harmonic basis expansion (Descoteaux et al., 2007). The ESR algorithm constructs a sampling design by modeling the acquisition directions as points on \mathbb{S}^2 and attempting to find a configuration which minimizes the electrostatic energy between point pairs. It has been widely used for constructing acquisition schemes over \mathbb{S}^2 , e.g., in the HCP. In this work, we used the ESR implementation from the *dipy* library (Garyfallidis et al., 2014). Without loss of generality, we considered diffusion signal in one voxel and assumed the signal has zero mean.

Let $\{\phi_j\}_{j=1}^J$ be the modified spherical harmonic basis. Within the space spanned by $\{\phi_j\}_{j=1}^J$, we generated eigenfunctions and eigenvalues as follows: eigenvalues were generated by $\rho_k = \exp(-0.2k)$ to mimic the decay phenomenon of the spectrum; the corresponding eigenfunctions were constructed from a random $J \times J$ orthogonal matrix \mathbf{B} according to $\psi_k(x) = \sum_{j=1}^J \mathbf{B}_{jk} \phi_j(x)$, for $k = 1, \dots, J$. We set $J = 45$ corresponding to a modified spherical

harmonic order of eight in accordance with the literature pertaining to the dMRI signal approximation (Hess et al., 2006). From these basis systems, we simulated two sets of random functions: the first one admits the GP assumption and the second one does not.

Under the *GP assumption*, for each simulated diffusion signal X_i , we sampled the coefficients corresponding to $\{\psi_k\}$ according to $\xi_{ik} \sim \mathcal{N}(0, \rho_k)$, $k = 1, 2, \dots, K$. Under the *non-GP assumption*, we sampled ξ_{ik} from a mixture distribution $\frac{1}{2} \mathcal{N}(-\sqrt{\rho_k/2}, \rho_k/2) + \frac{1}{2} \mathcal{N}(\sqrt{\rho_k/2}, \rho_k/2)$. This distribution has been used in several simulation studies in the FDA literature (Yao et al., 2005). To mimic the HCP acquisition protocol, we assumed signals X_i can be observed at 90 locations on \mathbb{S}^2 , and these locations were randomly sampled according to $(\theta, \phi) \sim \operatorname{Unif}(0, \pi) \times \operatorname{Unif}(0, 2\pi)$, which were then dispersed on the sphere using the ESR algorithm. The simulated X_i was then evaluated at each of these 90 locations and recorded with additive measurement error $\epsilon_{ij} \sim \mathcal{N}(0, \sigma^2)$. We considered $\sigma^2 = 0.1$ and 0.5 to simulate both high and low signal to noise ratios (SNR), respectively. This scheme was used to construct an independent training set, i.e., the simulated \mathcal{H} , and test set of sizes 100 and 50, respectively, for both the GP and non-GP cases.

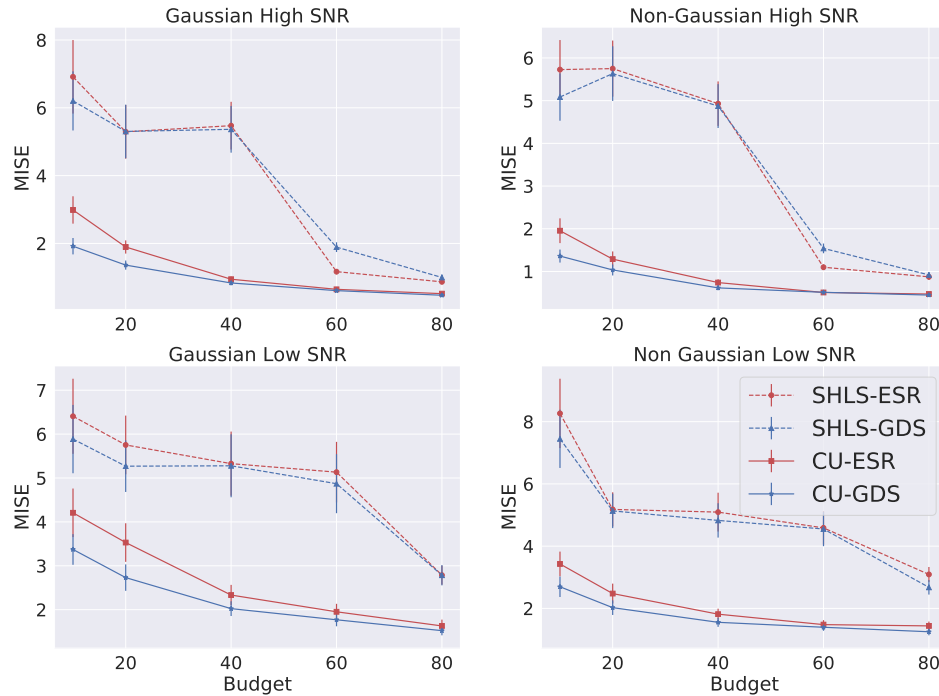


Fig 3: Mean integrated squared error and 95% standard error bars estimated with the test set for each of the four combinations of observation location selection and coefficient estimation.

We are interested in comparing the diffusion signal estimates under different approaches. The proposed greedy approach (Algorithm 1) is denoted as GDS (greedy design selector), and the proposed signal fitting in Equation (8) is denoted as CU (conditional expectation update). The penalized regression approach using the modified spherical harmonics from Section 3.1.1 is referred to as SHLS (spherical harmonic least squares). For both CU and GDS, the training data was used for prior summarization, as described in Section 3.1. For the SHLS fit, the regularization parameter was chosen via generalized cross validation. We evaluated the signal fit for each of the combined sampling and fitting methods (SHLS-ESR, SHLS-GDS, CU-ESR, and CU-GDS) over a sequence of increasing budgets by the integrated squared error (ISE) across the test set. For all methods, a modified spherical harmonic basis of order eight was used for fitting.

Figure 3 displays the test set performance of the four methods, for each combination of Gaussian vs. non Gaussian and high SNR vs. low SNR. Incorporating prior information into the coefficient estimation results in substantially better estimates, as both the CU-ESR and CU-GDS fits result in lower mean ISE (MISE) than SHLS-ESR and SHLS-GDS methods for all budgets and signal distributions considered. Moreover, the proposed method CU-GDS displays uniformly better performance than CU-ESR, indicating an additional increase in the quality of fits when the proposed diffusion signal function estimator is used in tandem with the proposed optimal design algorithm. The boost in performance is most significant in the sparse sample regime, e.g. $M \leq 40$. By comparing the results from SHLS-GDS and SHLS-ESR, we notice that the GDS design can be slightly detrimental to the fit quality if not coupled with the proposed CU estimator. This is expected since the GDS is derived under CU signal fitting and therefore in practice it is important to use them in conjunction. Additionally, we found the computational performance of CU-GDS fitting to be comparable with that of SHLS-ESR, see the supplemental material for more information.

5. REAL DATA EXPERIMENTS. We evaluated our method using diffusion data from the HCP. The full imaging acquisition and minimal diffusion MRI image preprocessing steps for HCP data are documented in [Glasser et al. \(2013\)](#). Briefly, all imaging was conducted on the 3T Siemens Connectom scanner (Erlangen, Germany). High-resolution T1w anatomical images were acquired with the 3D MPRAGE (magnetization prepared rapid gradient echo) sequence with a slice acceleration factor of 2 using 0.7 mm isotropic resolution. Diffusion imaging was performed using a 2D spin-echo EPI (echo planar imaging) sequence with approximately 90 diffusion directions at three non-zero b-values (1,000, 2,000, and 3,000 s/mm^2 each) and 6 $b = 0$ reference scans at 1.25 mm isotropic resolution. A full diffusion MRI run includes 6 runs of about 9 mins 50 seconds each, representing 3 acquisitions of different b-vectors, each acquired once with right-to-left (RL) and left-to-right (LR) phase encoding polarities; these are used to correct for susceptibility-induced distortion.

For our study, we randomly selected 240 healthy HCP subjects (age range: 20-35 years) to be used as training data, i.e. high resolution historical data \mathcal{H} . An additional 10 subjects from the same demographic were used as independent test data. A template of the diffusion data was created from the FA images of 20 randomly selected training subjects. Each subject's FA image was then warped to the template using the nonlinear registration algorithm in ANTs ([Avants et al., 2009](#)). A white matter mask was also applied in the template space. The $b = 1000$ shell of the training data was used to estimate the voxel specific diffusion functions for each subject. The estimates of the warping and diffusion functions for each training subject were used to construct mean and covariance functions at each voxel in the template space according to the procedure outlined in Section 3.1. The inverse warping function for each subject in the test data was used to map the template space mean and covariance functions into their subject space. For a sequence of increasing total budgets, we applied the GDS algorithm to select diffusion directions from the set of 90 $b = 1000$ vectors for each test subject independently. We determined an optimal set of directions to sample 1) for *each voxel*, and 2) for *an ROI*. For the second case, we randomly selected 10,000 voxels within the white matter mask to define the ROI \mathcal{V}_s . In analysis not reported here, we observed that the final results were insensitive to resamplings of \mathcal{V}_s , so long as the sample was sufficiently large. For diffusion signal function estimation, the GDS design was paired with the CU estimator and compared with the ESR design combined with the SHLS estimator.

Since in general, SHLS-ESR reconstruction enjoys good performance for dense samples, we first evaluated the diffusion signal estimation for both techniques at various sparse budgets by comparing them to the SHLS-ESR applied to the full 90 directions, denoted as SHLS-ESR90. Figure 4 displays boxplots of the ISE between the sparse sample reconstructions and SHLS-ESR90 over all of the white matter voxels, where CU-GDS-PV represents sampling scenario 1), and CU-GDS-COM represents sampling scenario 2). The CU-GDS framework produced reconstructions which better approximate the signal estimates of SHLS-ESR90 than does SHLS-ESR for each of the sparse budgets considered. The performance boost becomes more pronounced in the sparser cases, e.g., when we only have the budget to sample fewer than 20 directions (b-vectors). The per voxel design (CU-GDS-PV) resulted in lower average ISE than the per subject design (CU-GDS-COM), as expected since the latter is equivalent to the former with an additional constraint, but the difference is minimal relative to the performance of SHLS-ESR.

For each total budget considered, fODFs were constructed from the diffusion signal estimates by applying first the FRT and subsequently the spherical deconvolution algorithm from [Descoteaux et al. \(2009\)](#). Figure 5 displays the fODFs from a coronal slice of a randomly selected test subject. Visual inspection affirms that the fODFs generated from CU-GDS-COM more accurately model the directional information estimated from the full data. Using only 5 directions, CU-GDS-COM estimation already results in fODFs that very closely approximate

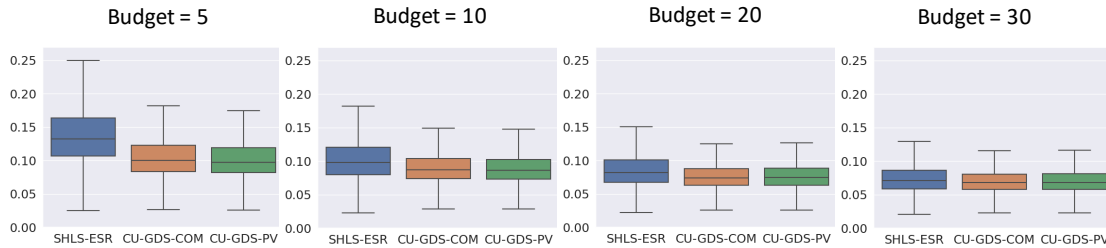


Fig 4: Boxplots of the ISE between the sparse sample reconstructions (SHLS-ESR, CU-GDS-COM, and CU-GDS-PV) and SHLS-ESR90, where CU-GDS-COM represents CU fit based on per subject design, and CU-GDS-PV represents CU fit based on per voxel design.

those based on the full set of 90 directions. For instance, the single fiber region in the corpus callosum (bottom left pink area) as well as the crossing fibers in the centrum semiovale (center blue area) are nearly identical between the budget = 5 and budget = 90 plots. This is not the case for SHLS-ESR, which struggles in both areas for sparse budgets. Boxplots of the per-voxel ISE between the sparse budget and full data reconstructions for both methods are displayed in the right column. For each sparse budget considered, the CU-GDS-COM produces estimates which more faithfully represent the full data reconstructions than does the SHLS-ESR.

The motivating application for this paper is to develop a sparse diffusion weighted signal sampling framework for brain structural connectome analysis. Therefore, we investigated the quality of the tractogram and structural connectivity resulting from the reconstructed fODFs at various sampling budgets. The tractogram was computed from the fODFs using the particle filtering tractography algorithm (Girard et al., 2014) that is implemented in *dipy* (Garyfalidis et al., 2014). Connectome matrices were reconstructed using the Desikan atlas (Desikan et al., 2006) created by FreeSurfer (Fischl, 2012). Figure 6 displays a visual comparison of the tractography results from SHLS-ESR and CU-GDS-COM for a set of increasing budgets, for a randomly selected test subject. We can see that with as few as 5 directions, the proposed methodology is able to produce meaningful streamlines, and the tractography results visually converge to the tractography using the full set of 90 directions quickly. The SHLS-ESR framework does not produce meaningful streamlines of the whole brain until a budget of 30 b-vectors or more. To quantify the structural connectivity matrix, we extracted and compared several graph topological metrics including network density, global efficiency, transitivity, and characteristic path length. Detailed definitions of these metrics as well as their interpretation within the context of connectome analysis can be found in (Rubinov and Sporns, 2010). Figure 7 displays the average and 95% errors bars for each of these metrics computed over the 10 subjects in the test set at different sampling budgets. We can see that the results of the CU-GDS-COM method converge to the full data results faster than the SHLS-ESR method. The SHLS-ESR generally needs 30 or more directions to obtain a connectivity matrix that is comparable with the one obtained from 90 directions, while the CU-GDS-COM only needs around 10.

Finally, we studied the ability of the proposed reconstruction method to capture meaningful variability across subjects. Due to the incorporation of a prior in the sampling direction selection and signal fitting, it is a valid concern that the CU-GDS could be “shrinking” the signal estimates too much towards the “average brain,” especially in the sparse sample case. To evaluate this, we leveraged the test and retest data in HCP, i.e., those HCP subjects that have multiple scans collected at different times. In total, 12 non training-set subjects with their test and retest diffusion data (24 scans) were involved in our analyses. Figure 8 shows

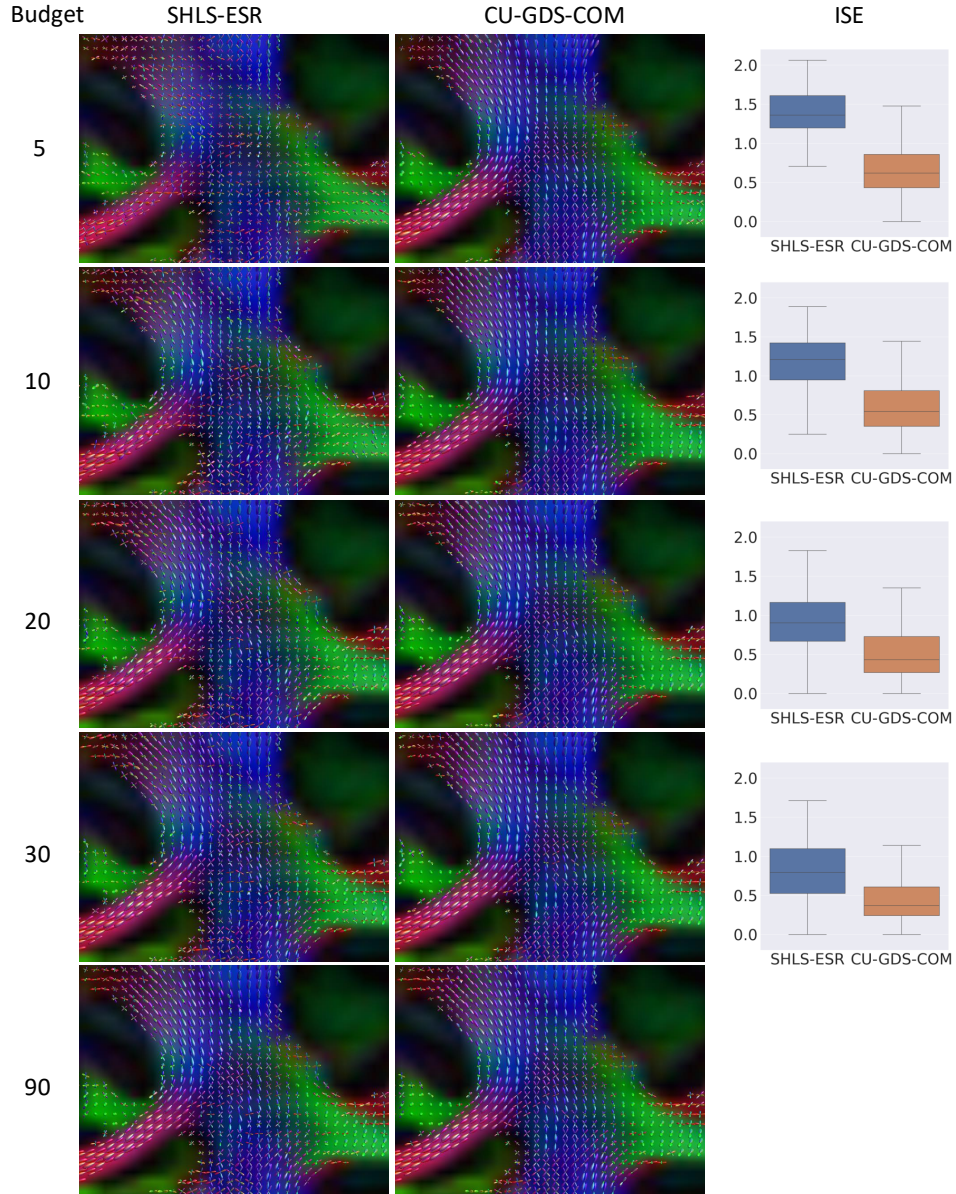


Fig 5: fODFs from a coronal slice of a randomly selected test subject reconstructed by SHLS-ESR (left column) and CU-GDS-COM (center column). The last column displays boxplots of the per voxel ISE between the sparse budget and full data reconstructions, for both methods. Each row corresponds to a different sampling budget.

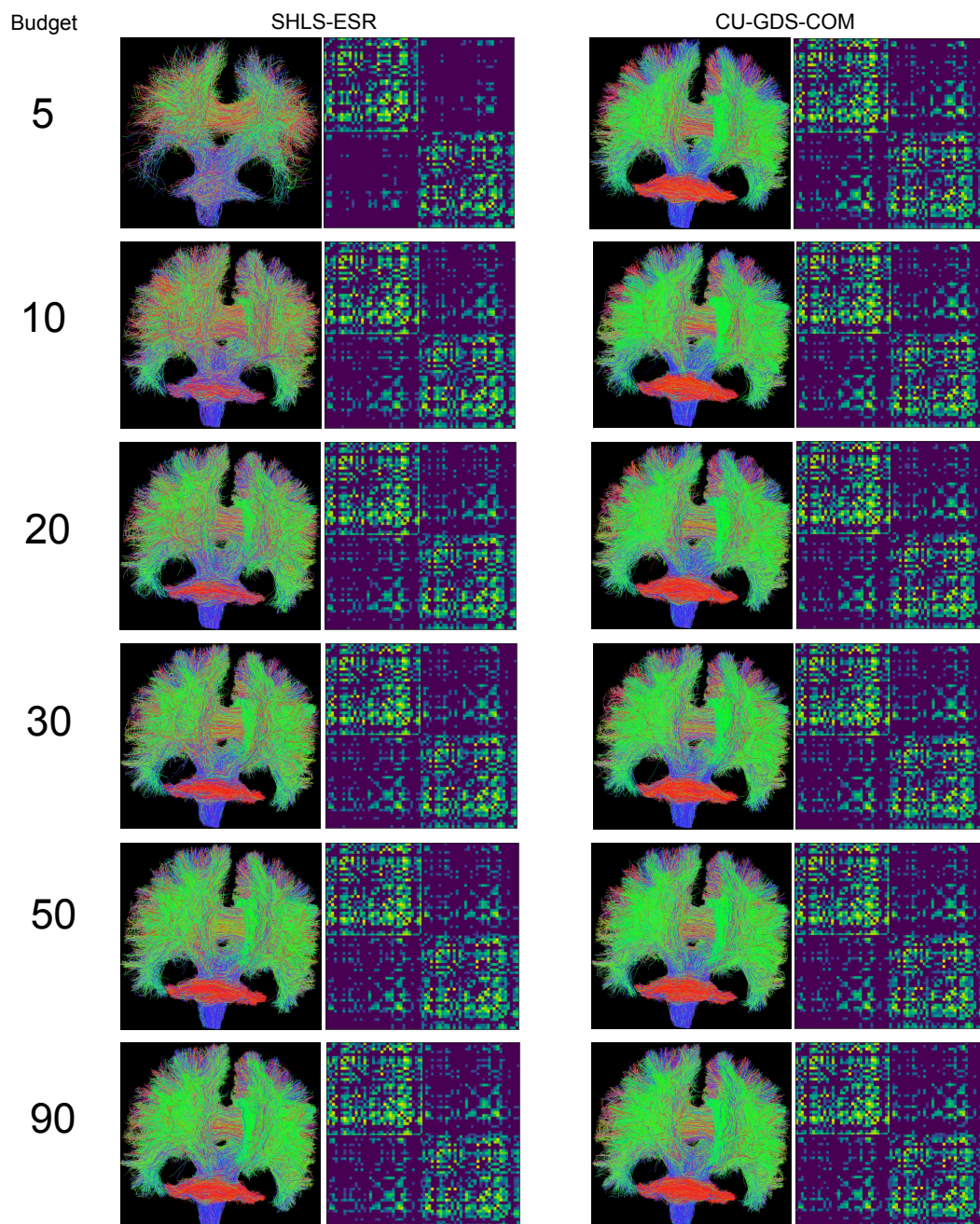


Fig 6: WM fiber streamlines and connectivity matrices from a randomly selected test subject. Tractography was run on fODFs constructed from diffusion signal function estimates from SHLS-ESR (left column) and CU-GDS-COM (right column) for a sequence of increasing total budgets.

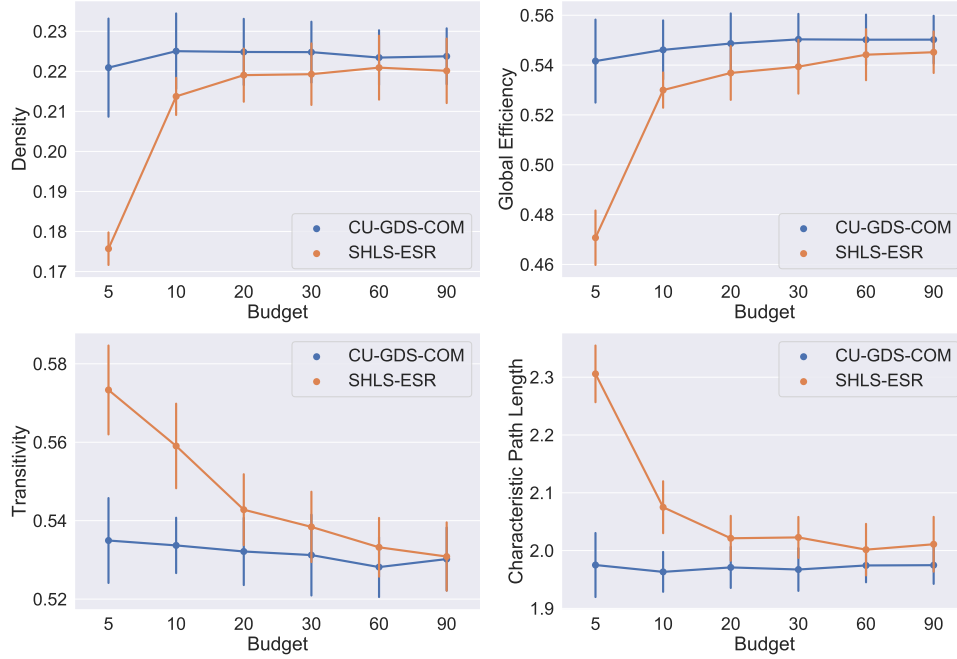


Fig 7: Graph topological metrics of brain networks computed based on SHLS-ESR and CU-GDS-COM methods over different budgets. Means and 95% error bars are displayed.

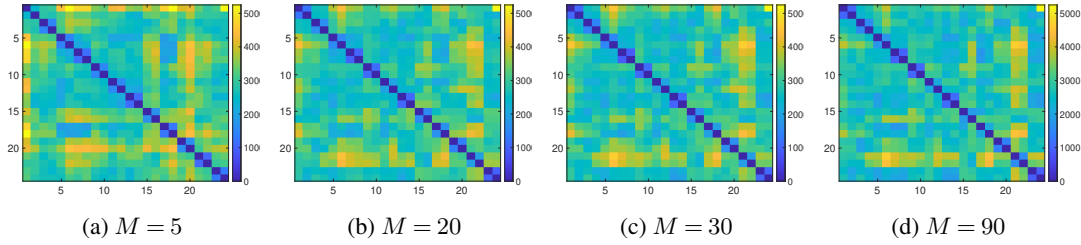


Fig 8: Each panel shows a pairwise distance matrix with elements being distances between connectivity matrices restored from the test and retest data of 12 HCP subjects using M diffusion directions. The diffusion signal is fitted based on CU-GDS-COM.

the pairwise distance matrices between the 24 connectivity matrices restored under different budgets. Note that we put data from the same subject next to each other to form a block pattern along the diagonal of the pairwise distance matrix. We see that even in sparse sample cases ($M \leq 30$), there are larger inter-subject (between subject) differences than intra-subject (within subjects) differences. Furthermore, the pairwise distance patterns for sparse cases are very similar to the dense case, indicating the proposed method can preserve inter-subject differences in sparse designs.

6. CONCLUSION AND DISCUSSION. This paper introduces a novel methodology which incorporates high-resolution historical dMRI data to optimize diffusion weighted directions in dMRI acquisition and sparse sample diffusion signal estimation. Historical data is used to construct a prior distribution of water diffusion at each voxel in a template space through a low-rank GP model. Given a new subject of interest for dMRI acquisition, the GP priors in the template space are mapped to the subject space and then used to define the

subject-specific acquisition directions that minimize the expected integrated squared error of the diffusion signal estimator. A computationally efficient greedy algorithm is proposed to select the directions and is shown to approximate the performance of the true optimal set of direction within some computable bounds. The mapped GP prior also serves an important role in defining the diffusion signal estimator from sparse samples. We show that the combination of the proposed diffusion sampling and signal estimation generally outperforms traditional techniques. The proposed framework is significantly better in the sparse sample case, i.e, when we only have limited budget in the number of diffusion directions to acquire. In applying the proposed method to analyze HCP data, we show the boost in performance of our method in diffusion signal estimation carries through to fODF reconstruction and ultimately to quality tractography estimation. The sparse sample tractography results are shown to both produce similar network characteristics as the densely sampled case, as well as capture meaningful variation between subjects.

Given the public availability of big brain imaging data sets with high-resolution dMRI, e.g., the different types of HCP sets, the Adolescent Brain Cognitive Development (ABCD) set, and the UK Biobank set, the requirement of finding a subset of subject’s data to serve in constructing the prior is easy to accomplish. In order to use our methodology for data acquisition of a new subject, a small number of $b = 0$ scans must first be collected to provide the subject’s coordinate for prior injection and to estimate the measurement error variance σ^2 . In this work, the registration between template and subject space was conducted using the FA image, but it is possible to instead use the $b = 0$ image for this purpose in a real application. For estimating the measurement error variance, although the historical sample could be used to estimate a global value for σ^2 , it is important to do so for each new subject since it captures the noise introduced by the scanner, which can vary substantially between machines and scanning sites. Typically, only a few initial $b = 0$ acquisitions are required for a sufficiently good estimation of σ^2 , and the proposed method is robust to some degree of bias in the estimate (see the supplemental material for further discussion).

We offer a couple potential applications of the proposed framework. First, in clinical scans, long scanning times can be infeasible for a variety of reasons. The proposed method can be used to design optimal gradients to quickly acquire sparse q-space data for structural connectome study for important clinical purposes such as surgical planning. Second, there are studies trying to increase the spatial resolution of diffusion MRI to more accurately detect white matter fiber tracts at a submillimeter isotropic resolution (Chang et al., 2015). Such spatial resolution increase is at the cost of reduced q-space resolution (e.g., only around 12 diffusion directions were acquired in Chang et al. (2015)) and increased scanning time. Given our method’s outstanding performance in the sparse sampling case, this is an ideal application scenario: with 12 or fewer samples, our method can produce similar tractography results and connectomes as data with 60 or more samples.

This work can be extended in several interesting directions. Right now, we only consider data on a single shell, so one extension is to augment the statistical model to accommodate for signal attenuation in the multi-shell situation. This would allow the derivation of a joint optimization scheme for both gradient direction and magnitude in the dMRI protocol. Another extension involves multi-voxel analysis and information borrowing from neighborhood regions. The white matter tracts often group in bundles that span many voxels, inducing correlations between the signal in neighboring voxels. Considering such correlation can increase the efficiency of the estimation procedure.

7. SUPPLEMENTARY MATERIALS. The supplementary materials include further elaborations and proofs of the results presented.

REFERENCES

- Alexander, D., G. Barker, and S. Arridge (2002). Detection and modeling of non-gaussian apparent diffusion coefficient profiles in human brain data. *Magnetic Resonance in Medicine* 48(2), 331–340.
- Andersson, J. L. and S. N. Sotiropoulos (2015). Non-parametric representation and prediction of single- and multi-shell diffusion-weighted MRI data using Gaussian processes. *NeuroImage* 122, 166 – 176.
- Arsigny, V., P. Fillard, X. Pennec, and N. Ayache (2007). Geometric means in a novel vector space structure on symmetric positive-definite matrices. *SIAM Journal on Matrix Analysis and Applications* 29(1), 328–347.
- Avants, B. B., C. L. Epstein, M. Grossman, and J. C. Gee (2008, Feb). Symmetric diffeomorphic image registration with cross-correlation: evaluating automated labeling of elderly and neurodegenerative brain. *Medical Image Analysis* 12(1), 26–41.
- Avants, B. B., N. Tustison, and G. Song (2009). Advanced normalization tools (ants). *Insight Journal* 2(365), 1–35.
- Basser, P., J. Mattiello, and D. Lebihan (1994). Estimation of the effective self-diffusion tensor from the NMR spin echo. *Journal of Magnetic Resonance, Series B* 103, 247–254.
- Caruyer, E. and R. Deriche (2009, September). Adaptive design of sampling directions in diffusion tensor MRI and validation on human brain images. In *MICCAI Workshop on Diffusion Modelling and the Fiber Cup*, Londres, United Kingdom.
- Chamon, L. and A. Ribeiro (2017). Approximate supermodularity bounds for experimental design. In *Advances in Neural Information Processing Systems*, Volume 30, pp. 5403–5412.
- Chang, H.-C., M. Sundman, L. Petit, S. Guhaniyogi, M.-L. Chu, C. Petty, A. W. Song, and N.-k. Chen (2015). Human brain diffusion tensor imaging at submillimeter isotropic resolution on a 3 Tesla clinical MRI scanner. *Neuroimage* 118, 667–675.
- Chen, N.-K., A. Guidon, H.-C. Chang, and A. W. Song (2013). A robust multi-shot scan strategy for high-resolution diffusion weighted MRI enabled by multiplexed sensitivity-encoding (MUSE). *Neuroimage* 72, 41–47.
- Descoteaux, M., E. Angelino, S. Fitzgibbons, and R. Deriche (2007). Regularized, fast, and robust analytical Q-ball imaging. *Magnetic Resonance in Medicine* 58, 497–510.
- Descoteaux, M., R. Deriche, T. R. Knösche, and A. Anwander (2009). Deterministic and probabilistic tractography based on complex fibre orientation distributions. *IEEE Transactions on Medical Imaging* 28, 269–286.
- Desikan, R. S., F. Ségonne, B. Fischl, B. T. Quinn, B. C. Dickerson, D. Blacker, R. L. Buckner, A. M. Dale, R. P. Maguire, B. T. Hyman, M. S. Albert, and R. J. Killiany (2006). An automated labeling system for subdividing the human cerebral cortex on MRI scans into gyral based regions of interest. *NeuroImage* 31, 968–980.
- Dryden, I. L., A. Koloydenko, and D. Zhou (2009, 09). Non-Euclidean statistics for covariance matrices, with applications to diffusion tensor imaging. *Ann. Appl. Stat.* 3(3), 1102–1123.
- Fischl, B. (2012). FreeSurfer. *NeuroImage* 62, 774–781.
- Gao, T., S. Kovalsky, D. Boyer, and I. Daubechies (2018, 02). Gaussian process landmarking on manifolds. *SIAM Journal on Mathematics of Data Science* 1.
- Garyfallidis, E., M. Brett, B. Amirbekian, A. Rokem, S. Van Der Walt, M. Descoteaux, and I. Nimmo-Smith (2014). Dipy, a library for the analysis of diffusion mri data. *Frontiers in Neuroinformatics* 8, 8.
- Girard, G., K. Whittingstall, R. Deriche, and M. Descoteaux (2014). Towards quantitative connectivity analysis: Reducing tractography biases. *NeuroImage* 98, 266–278.
- Glasser, M. F., S. M. Smith, D. S. Marcus, J. L. Andersson, E. J. Auerbach, T. E. Behrens, T. S. Coalson, M. P. Harms, M. Jenkinson, S. Moeller, E. C. Robinson, S. N. Sotiropoulos, J. Xu, E. Yacoub, K. Ugurbil, and D. C. Van Essen (2016). The Human Connectome Project’s neuroimaging approach. *Nature Neuroscience* 19(9), 1175–1187.
- Glasser, M. F., S. N. Sotiropoulos, J. A. Wilson, T. S. Coalson, B. Fischl, J. L. Andersson, J. Xu, S. Jbabdi, M. Webster, J. R. Polimeni, D. C. V. Essen, M. Jenkinson, and f. t. W.-M. H. Consortium (2013). The minimal preprocessing pipelines for the Human Connectome Project. *NeuroImage* 80, 105–124.
- Golub, G. H., M. Heath, and G. Wahba (1979). Generalized cross-validation as a method for choosing a good ridge parameter. *Technometrics* 21(2), 215–223.
- Hess, C. P., P. Mukherjee, E. T. Han, D. Xu, and D. B. Vigneron (2006). Q-ball reconstruction of multimodal fiber orientations using the spherical harmonic basis. *Magnetic Resonance in Medicine* 56, 104–117.
- Hsing, T. and R. Eubank (2013, 01). *Theoretical Foundations of Functional Data Analysis, with an Introduction to Linear Operators*. Wiley.
- James, G. M., T. J. Hastie, and C. A. Sugar (2000). Principal component models for sparse functional data. *Biometrika* 87(3), 587–602.
- Ji, H. and H.-G. Müller (2017). Optimal designs for longitudinal and functional data. *Journal of the Royal Statistical Society: Series B (Statistical Methodology)* 79(3), 859–876.

- Jones, D., M. Horsfield, and A. Simmons (1999). Optimal strategies for measuring diffusion in anisotropic systems by magnetic resonance imaging. *Magnetic Resonance in Medicine* 42(3), 515–525.
- Karhunen, K. (1946). Zur spektraltheorie stochastischer prozesse. *Ann. Acad. Sci. Fennicae, AI* 34.
- Maier-Hein, K. H., P. F. Neher, J.-C. Houde, M.-A. Côté, E. Garyfallidis, J. Zhong, M. Chamberland, F.-C. Yeh, Y.-C. Lin, Q. Ji, et al. (2017). The challenge of mapping the human connectome based on diffusion tractography. *Nature Communications* 8(1), 1–13.
- Mardia, K., J. Kent, and J. Bibby (1979). *Multivariate Analysis*. Probability and mathematical statistics. London: Acad. Press.
- Poot, D. H. J., A. J. den Dekker, E. Achten, M. Verhoye, and J. Sijbers (2010). Optimal experimental design for diffusion kurtosis imaging. *IEEE Transactions on Medical Imaging* 29(3), 819–829.
- Quiñonero-Candela, J. and C. E. Rasmussen (2005). *Analysis of Some Methods for Reduced Rank Gaussian Process Regression*, pp. 98–127. Berlin, Heidelberg: Springer Berlin Heidelberg.
- Rubinov, M. and O. Sporns (2010). Complex network measures of brain connectivity: Uses and interpretations. *NeuroImage* 52, 1059–1069.
- Stejskal, E. O. and J. E. Tanner (1965). Spin diffusion measurements: spin echoes in the presence of a time dependent field gradient. *The Journal of Chemical Physics* 42, 288–292.
- Tournier, J.-D., F. Calamante, and A. Connelly (2012). Mrtrix: Diffusion tractography in crossing fiber regions. *International Journal of Imaging Systems and Technology* 22(1), 53–66.
- Tuch, D. S. (2004). Q-ball imaging. *Magnetic Resonance in Medicine* 52, 1358–1372.
- Tuch, D. S., T. G. Reese, M. R. Wiegell, N. Makris, J. W. Belliveau, and V. J. Wedeen (2002). High angular resolution diffusion imaging reveals intravoxel white matter fiber heterogeneity. *Magnetic Resonance in Medicine* 48(4), 577–582.
- Tuch, D. S., T. G. Reese, M. R. Wiegell, and V. J. Wedeen (2003). Diffusion MRI of complex neural architecture. *Neuron* 40, 885–895.
- Wu, M., A. Diez-Roux, T. E. Raghunathan, and B. N. Sánchez (2018). FPCA-based method to select optimal sampling schedules that capture between-subject variability in longitudinal studies. *Biometrics* 74(1), 229–238.
- Yao, F., H.-G. Müller, and J.-L. Wang (2005). Functional data analysis for sparse longitudinal data. *Journal of the American Statistical Association* 100(470), 577–590.

Supplemental Materials for “Optimized Diffusion Imaging for Brain Structural Connectome Analysis”

APPENDIX S1: MODIFIED SPHERICAL HARMONIC BASIS FUNCTIONS

This section provides additional exposition on the diffusion signal estimation procedure outlined in Section 3.1.1 of the main text.

The spherical harmonics are defined as follows

$$Y_l^m(\theta_1, \theta_2) = \sqrt{\frac{(2l+1)(l-m)!}{4\pi(l+m)!}} P_l^m(\cos(\theta_1)) e^{im\theta_2},$$

where the polar angle $\theta_1 \in [0, \pi]$ and azimuthal angle $\theta_2 \in [0, 2\pi]$, P_l^m are the Legendre polynomials with order indices $l = 0, 1, \dots$, and phase factors $m = -l, \dots, 0, \dots, l$. The spherical harmonics form a complete orthogonal basis system for $\mathbb{L}^2(\mathbb{S}^2)$. A real-valued and symmetric basis that is suitable for modeling diffusion signals can be constructed from the spherical harmonics according to

$$(S.1) \quad \phi_j = \begin{cases} \sqrt{2}\text{Re}(Y_k^m) & -k \leq m < 0 \\ Y_k^0 & m = 0 \\ \sqrt{2}\text{Im}(Y_k^m) & 0 < m \leq k \end{cases}$$

for $k = 0, 2, 4, \dots, l$, $m = -k, \dots, 0, \dots, k$ and $j = (k^2 + k + 2)/2 + m$, where the total number of basis functions is $J = (l+1)(l+2)/2$.

To protect against over-fitting, it is important to promote smoother solutions. For function approximation on some Euclidean space, this is typically accomplished by penalizing the \mathbb{L}^2 norm of the Laplacian applied to the candidate fit. The Laplace-Beltrami operator is a generalization of the Laplacian to submanifolds of Euclidean space. It has an especially simple form for the spherical harmonics, satisfying the relationship $\Delta_{\mathbb{S}^2} Y_l^m = -l(l+1)Y_l^m$, where $\Delta_{\mathbb{S}^2}$ denotes the Laplace-Beltrami operator on \mathbb{S}^2 . Coupling this with the orthonormality of (S.1), it follows that for any $g \in \text{span}\{\phi_j\}_{j=1}^J$, $\|\Delta_{\mathbb{S}^2} g\|_{\mathbb{L}^2}^2 = \mathbf{c}_g^\top \mathbf{R} \mathbf{c}_g$, where $\mathbf{R} = \text{Diag}(l_1^2(l_1+1)^2, \dots, l_J^2(l_J+1)^2)$ with l_j being the order associated with basis function ϕ_j , and $\mathbf{c}_g \in \mathbb{R}^J$ being the coordinates of g with respect to $\phi(p) = (\phi_1(p), \dots, \phi_J(p))^\top$.

For voxel v in subject i , its diffusion signal can be estimated by solving the following regularized least squares problem

$$\hat{\mathbf{c}}_{vi} = \underset{\mathbf{c} \in \mathbb{R}^J}{\text{argmin}} \sum_{m=1}^{M_i} (s_{vim} - \mathbf{c}^\top \phi(p_{im}))^2 + \lambda_i \int_{\mathbb{S}^2} (\Delta_{\mathbb{S}^2}(\mathbf{c}^\top \phi(p)))^2 dp,$$

for penalty $\lambda_i > 0$. Denoting the $M_i \times J$ matrix of basis function evaluations $[\Phi_i]_{mj} = \phi_j(p_{im})$ and the vector of observed signal $\mathbf{s}_{vi} = (s_{vi1}, \dots, s_{viM_i})^\top$. This optimization problem has a closed form solution:

$$\hat{\mathbf{c}}_{vi} = [\Phi_i^\top \Phi_i + \lambda_i \mathbf{R}]^{-1} \Phi_i^\top \mathbf{s}_{vi},$$

and the resulting smoothed estimate of diffusion signal is given by $\hat{X}_{vi}(p) = \hat{\mathbf{c}}_{vi}^\top \phi(p)$ at $p \in \mathbb{S}^2$.

The roughness penalty parameter λ_i controls the trade-off between the candidate solution's fit to the observed data and its “wigglyness.” In the literature, the penalty parameter is typically chosen through either cross validation or by minimizing the generalized cross validation criteria (GCV), which can be interpreted as an estimator of the expected predicted residual error sum of squares from leave-one-out cross validation (Golub et al., 1979). In this work, we opted for the GCV primarily due to its computational efficiency, a property that is paramount given the massive data size encountered in a whole brain dMRI study.

APPENDIX S2: MEASUREMENT ERROR VARIANCE ESTIMATION

Our statistical model for the observed diffusion signal, normalized with respect to the mean non diffusion weighted signal, i.e. mean $b = 0$ signal, assumes that the measurement error is independent of both b -vector and b -value. Let μ_v^0 be the true non-diffusion weighted signal in voxel v and let s_{vl}^0 be l -th ($l = 1, \dots, n$) $b = 0$ diffusion signal measurement at voxel v . Then the natural extension of our statistical model to the $b = 0$ data is given by

$$s_v^0/\mu_v^0 = 1 + \epsilon$$

where $\epsilon \sim N(0, \sigma^2)$ is the measurement error variance. Hence, the distribution of the $b = 0$ signal is $s_v^0 \sim N(\mu_v^0, [\mu_v^0]^2 \sigma^2)$ and we choose to estimate σ^2 with

$$\hat{\sigma}^2 = \frac{1}{|\mathcal{V}|} \sum_{v \in \mathcal{V}} \widehat{\text{Var}}(s_v^0)/(\bar{s}_v^0)^2,$$

where $\widehat{\text{Var}}(s_v^0)$ is the empirical variance of measurements $s_{v1}^0, \dots, s_{vn}^0$ and \bar{s}_v^0 is the empirical mean.

We investigate the properties of $\hat{\sigma}^2$ under the extension of the statistical model for the $b = 0$ diffusion signal. Using a multivariate Taylor expansion and truncating after the first order terms, it is easy to show that

$$(S.2) \quad \mathbb{E} \left[\frac{\widehat{\text{Var}}(s_v^0)}{(\bar{s}_v^0)^2} \right] \approx \frac{\mathbb{E}[\widehat{\text{Var}}(s_v^0)]}{\mathbb{E}[(\bar{s}_v^0)^2]}$$

Since $\bar{s}_v^0 \sim N(\mu_v^0, [\mu_v^0]^2 \sigma^2/n)$, we have $\mathbb{E}[(\bar{s}_v^0)^2] = \text{Var}(\bar{s}_v^0) + \mathbb{E}[\bar{s}_v^0]^2 = (\mu_v^0)^2(\sigma^2/n + 1)$ and $\mathbb{E}[\widehat{\text{Var}}(s_v^0)]$ is an unbiased estimator of $[\mu_v^0]^2 \sigma^2$. Plugging these back into (S.2) we obtain the approximation

$$\mathbb{E} \left[\frac{\widehat{\text{Var}}(s_v^0)}{(\bar{s}_v^0)^2} \right] \approx \frac{\sigma^2}{\sigma^2/n + 1}$$

Again using the first order Taylor approximation, we obtain the following approximation for the variance

$$\text{Var} \left[\frac{\widehat{\text{Var}}(s_v^0)}{(\bar{s}_v^0)^2} \right] \approx \left(\frac{\sigma^2}{\sigma^2/n + 1} \right)^2 \left[\frac{2}{n-1} + 2(1 - (\sigma^2/n + 1)^{-2}) \right]$$

Therefore, we obtain the following approximations of the mean and variance of $\hat{\sigma}^2$,

$$\mathbb{E}[\hat{\sigma}^2] \approx \frac{\sigma^2}{\sigma^2/n + 1}$$

and

$$\text{Var}(\hat{\sigma}^2) \approx \frac{1}{|\mathcal{V}|} \left(\frac{\sigma^2}{\sigma^2/n + 1} \right)^2 \left[\frac{2}{n-1} + 2(1 - (\sigma^2/n + 1)^{-2}) \right]$$

The approximate bias of the estimator is given by

$$\mathbb{E}[\hat{\sigma}^2] - \sigma^2 \approx \sigma^2 \left[\frac{1}{\sigma^2/n + 1} - 1 \right]$$

and therefore, while the estimator is asymptotically unbiased, we expect some finite sample downward bias. The variance decays like $|\mathcal{V}|^{-1}$, which is typically very small (i.e. we average over many voxels) and hence the estimator is stable.

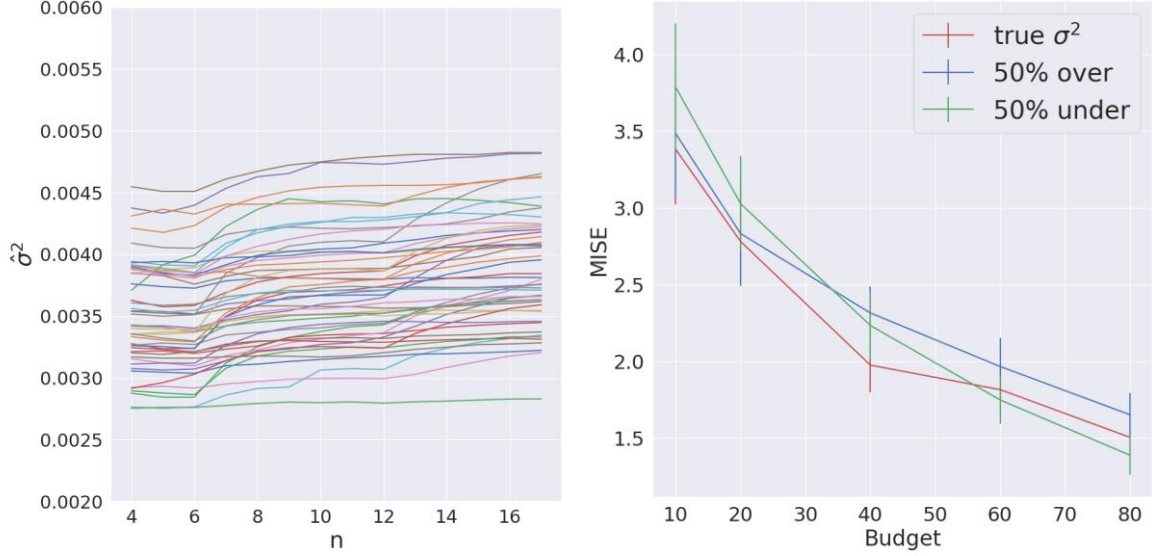


Fig S1: (left) Estimates of the measurement error variance for 50 randomly selected training subjects over a sequence of increasing number of $b = 0$ images. (right) MISE and 95% errors bars of CU-GDS reconstructions computed over the Gaussian low SNR simulation data using exact σ^2 (red), and 50% over and under estimations (blue and green).

In practical applications we assume that n , the number of $b = 0$ images in the pre-scanning period, is small and therefore we expect to incur some bias as a result. To assess this bias in practice, we studied the estimator's performance on each of the subjects in the high resolution historical training set. Each subject has a total of $n = 18$ $b = 0$ images and for each $j = 4, 5, \dots, n$, we selected j of the subject's $b = 0$ images and applied the estimator $\hat{\sigma}^2$. The left panel of figure S1 displays the results for a sample of 50 randomly selected subjects. As predicted, the small sample estimate appear to have slight downward bias. That said, comparing the estimates using only 4 $b = 0$ to the full set of $n = 18$; 33 (66%) are within 10% of the final estimated value and, 47 (94%) are within 20% and all are within 25%.

To assess the proposed method's sensitivity to bias in the estimation of σ^2 , we used the Gaussian low SNR simulation set-up from Section 4 and compared the reconstruction performance of CU-GDS when σ^2 is both under and overestimated by 50%. The right panel of figure S1 shows that there is not much degradation in performance, as measured by the mean ISE across the test set, as the biased reconstructions still outperform all other reconstruction methods in the sparse sample case (compare to bottom left panel in figure 2).

APPENDIX S3: BAYESIAN PERSPECTIVE OF DIFFUSION SIGNAL ESTIMATION FROM SPARSE DATA

The derivation of equation (7) can be motivated from a fully Bayesian perspective. From the Bayes rule, the posterior distribution of the coefficients

$$P(\xi_K | s_M, P_M, \mathcal{H}) \propto P(s_M | P_M, \xi_K) P(\xi_K | \mathcal{H})$$

where the prior $P(\xi_K | \mathcal{H}) \sim \mathcal{N}(\mathbf{0}, \mathbf{\Lambda})$ is empirically estimated from \mathcal{H} , and the likelihood $s_M | \xi_K$ follows a multivariate Gaussian distribution $\mathcal{N}(\mu_M + \Psi_{M,K} \xi_K, \sigma^2 \mathbf{I}_M)$, which can be derived from equation (3). It is easy to show that the mean of this posterior distribution is exactly the conditional expectation in (7). Equivalently, we can consider the joint distribution

of the observations and the process at a new point, i.e. the distribution of the random vector $(\mathbf{s}_M, X(p))^\top$. Through conditioning arguments on the resulting joint Gaussian distribution, the posterior predictive distribution for $X(p)$ can be shown to have mean

$$\mu(p) + (C(p_1, p), \dots, C(p_M, p))^\top \left[\begin{pmatrix} C(p_1, p_1) & \dots & C(p_1, p_M) \\ \vdots & & \vdots \\ C(p_M, p_1) & \dots & C(p_M, p_M) \end{pmatrix} + \sigma^2 \mathbf{I}_M \right]^{-1} (\mathbf{s}_M - \boldsymbol{\mu}_M)$$

Assuming the reduced rank approximation of the covariance function C in terms of the first K eigenvalue-eigenfunction pairs, it is easy to show that the above is equivalent to equation (8).

APPENDIX S4: OPTIMAL Q-SPACE SAMPLING

S4.1. Proof of Theorem 1.

LEMMA 1. *Define the auxiliary function*

$$f(\mathbf{P}_M) = \text{trace}((\boldsymbol{\Lambda}_K^{-1} + \frac{1}{\sigma^2} \boldsymbol{\Psi}_{M,K}^\top \boldsymbol{\Psi}_{M,K})^{-1}) - \text{trace}(\boldsymbol{\Lambda}_K)$$

The maximization problem (12) is equivalent to the minimization problem

$$(S.3) \quad \mathbf{P}_M^* = \underset{\mathbf{P}_M \in \mathcal{P}_M(\mathcal{A})}{\text{argmin}} f(\mathbf{P}_M)$$

PROOF. Using the Woodbury identity, we have that

$$\boldsymbol{\Lambda}_K - \boldsymbol{\Lambda}_K \boldsymbol{\Psi}_{M,K}^\top [\boldsymbol{\Psi}_{M,K} \boldsymbol{\Lambda}_K \boldsymbol{\Psi}_{M,K}^\top + \sigma^2 \mathbf{I}_M]^{-1} \boldsymbol{\Psi}_{M,K} \boldsymbol{\Lambda}_K = (\boldsymbol{\Lambda}_K^{-1} + \frac{1}{\sigma^2} \boldsymbol{\Psi}_{M,K}^\top \boldsymbol{\Psi}_{M,K})^{-1}$$

Taking the trace of both sides shows $g(\mathbf{P}_M) = -f(\mathbf{P}_M)$ and the result follows. \square

LEMMA 2. *Let f be defined as in Lemma 1, then*

$$f(\hat{\mathbf{P}}_m^*) \leq \left[1 - \exp \left(-\frac{\rho_1^{-1}}{\rho_K^{-1} + \frac{m}{\sigma^2} \lambda_\phi^*} \frac{m}{M} \right) \right] f(\mathbf{P}_M^*)$$

PROOF OF LEMMA 1. The matrix $(\boldsymbol{\Lambda}_K^{-1} + \frac{1}{\sigma^2} \boldsymbol{\Psi}_{M,K}^\top \boldsymbol{\Psi}_{M,K})^{-1}$ is the covariance of the posterior distribution of $\boldsymbol{\xi}_K$ given the prior $P(\boldsymbol{\xi}_K | \mathcal{H}) \equiv \mathcal{N}(\mathbf{0}, \boldsymbol{\Lambda}_K)$ and $P(\epsilon | \sigma^2) \equiv \mathcal{N}(\mathbf{0}, \sigma^2 \mathbf{I}_M)$ under the reduced rank GP model. Therefore, (S.3) defines the A-optimal design for (7), the MAP estimator of $\boldsymbol{\xi}_K$. Using Theorems 1 and 3 from Chamon and Ribeiro (2017) and Lemma 1 above, it is easy to see that

$$f(\hat{\mathbf{P}}_m^*) \leq \left[1 - \exp \left(-\frac{\bar{\alpha} m}{M} \right) \right] f(\mathbf{P}_M^*)$$

where

$$\begin{aligned} \bar{\alpha} &= \min_{l \leq m} \frac{\lambda_{\min}(\boldsymbol{\Lambda}_K^{-1})}{\lambda_{\max}(\boldsymbol{\Lambda}_K^{-1}) + \frac{l}{\sigma^2} \lambda_\psi^*} \\ &= \frac{\rho_1^{-1}}{\rho_K^{-1} + \frac{m}{\sigma^2} \lambda_\psi^*} \end{aligned}$$

giving the desired result. \square

PROOF OF THEOREM 1. The result follows immediately from Lemma 2 using the identity $f(\mathbf{P}_M) = -g(\mathbf{P}_M)$. \square

S4.2. Interpretation of the Performance Bound. To facilitate interpretation, assume that we have run Algorithm 1 for M iterations. Using the bound from Theorem 1, we have the ratio

$$\frac{g(\hat{\mathbf{P}}_M^*)}{g(\mathbf{P}_M^*)} \geq \left[1 - \exp \left(- \left(\frac{\rho_K}{\rho_1} \right) \left(1 + M\lambda_\psi^* \left(\frac{\rho_K}{\sigma^2} \right) \right)^{-1} \right) \right].$$

We now explore how this bound behaves in different scenarios. Consider that the ranges of terms in the exponential component are $\frac{\rho_K}{\rho_1} \in (0, 1)$, and $(1 + M\lambda_\psi^* (\frac{\rho_K}{\sigma^2}))^{-1} \in (0, 1)$. The bound reaches its tightest, $1 - \exp(-1)$, as both terms approach 1. Alternatively, the bound is loosest, approaching the trivial bound of 0, when either of the terms approaches 0. We have the following interpretations. In terms of the random function X , the bound is tighter when the eigenvalues of the reduced rank covariance function are clustered near to one another. In other words, the functional variation is nearly uniformly distributed among the $\{\psi_1, \dots, \psi_K\}$, i.e. there is large uncertainty in the underlying local diffusion direction. Additionally, due to the connection between the trace of a matrix and its eigenvalues, we have that $\lambda_\psi^* = \max_{p \in \mathcal{A}} \sum_{k=1}^K \psi_k^2(p)$, which is clearly bounded by $\sum_{k=1}^K \|\psi_k\|_\infty^2$. Since the sup-norm increases with higher order spherical harmonics, very large values of $\|\psi_k\|_\infty$ indicate a relatively large coefficient on a high order ϕ_j . Said another way, the less the contribution of high order components to the ψ_k 's, the tighter the bound on the ratio between the approximate and globally optimal designs. Finally, notice that when $\frac{\rho_K}{\sigma^2}$ is large, the second term in the exponential goes to 0. Therefore, the bound is tighter when the signal to noise ratio is low.

APPENDIX S5: COMPUTATION SPEED COMPARISON

The computational speed of the *dipy* implementation of the ESR algorithm and our implementation of Algorithm 1 (GDS) were compared over a sequence of increasing total budgets. The comparisons were run on a machine with 1.80 GHz CPU and 16 GB of RAM 10 times for each budget. Table 1 displays the mean compute time for both methods at each budget considered, along with the standard deviation in parentheses. The results show that the GDS is reasonably fast, which is critically important in practice since we need to calculate the optimal gradient table for each subject of interest in real time before the diffusion imaging. The computational performance of the GDS and ESR are comparable, though the latter need not be computed per-subject.

Budget	Computational Time (s)	
	ESR	GDS
10	0.4299 (0.0201)	0.7584 (0.0159)
20	0.7405 (0.0272)	1.1068 (0.0487)
30	1.1755 (0.0194)	1.3890 (0.0061)
50	2.7060 (0.0820)	2.2080 (0.0677)
70	4.9674 (0.1823)	3.6329 (0.1754)
90	7.6678 (0.0789)	6.1353 (0.1289)

TABLE 1

Computation speed comparison between GDS and ESR design selection algorithms for a sequence of increasing budgets.